Measurements of Electric Field Noise and Light-Induced Charging in Cryogenic Surface Electrode Ion Traps

MASSACHUSETTS INSTITUTE OF TECHNOLOGY
AUG 13 2010
LIBRARIES

by

Nathan S. Lachenmyer

Submitted to the Department of Physics
in partial fulfillment of the requirements for the degree of

Bachelor of Science in Physics

ARCHIVES

at the

MASSACHUSETTS INSTITUTE OF TECHNOLOGY

June 2010

© Nathan S. Lachenmyer, MMX. All rights reserved.

The author hereby grants to MIT permission to reproduce and distribute publicly paper and electronic copies of this thesis document in whole or in part.

Author .....
Department of Physics
May 21, 2010

Certified by .....
Isaac L. Chuang
Professor of Physics
Thesis Supervisor

Accepted by .....
David Pritchard
Thesis Coordinator

Measurements of Electric Field Noise and Light-Induced Charging in Al and Cu Surface Electrode Ion Traps at Cryogenic Temperatures

by

Nathan S. Lachenmyer

Submitted to the Department of Physics
on May 21, 2010, in partial fulfillment of the
requirements for the degree of
Bachelor of Science in Physics

Abstract

Ion traps provide an excellent tool for controlling and observing the state of a single trapped ion. For this reason, ion traps have been proposed as a possible system for large-scale quantum computation. However, many obstacles must be overcome before quantum computing can become a reality. In particular, perturbations in the electric field due to noise and electrode charging must be reduced to increase coherence of the motional quantum state. Gold has been a popular choice in the past due to its inert properties; however, it is undesireable due its incompatibility with CMOS technology. This has led to increased research into alternative CMOS-compatible materials, such as aluminum and copper.

This thesis presents measurements of electric field noise and light-induced charging in aluminum, copper, and gold surface electrode traps. In addition, the effect of oxide growth on field noise and electrode charging is explored by controlling the thickness of aluminum oxide on several aluminum traps. The measurements show that electric field noise can be suppressed in aluminum traps to approximately 10^{-18} V^2 cm^{-2} Hz^{-1}, matching the noise exhibited in gold traps, and that copper traps exhibit noise within an order of magnitude of that in aluminum and gold. However, the natural oxide of aluminum poses many problems towards high-performance aluminum ion traps. The electric field noise is shown to be strongly dependent on the oxide thickness, increasing the noise by a factor of about 10 until saturation at a thickness of 13 nm. Charging of surface electrodes is shown to be highly dependent upon the material, but the model presented does not match the experimental data and is found to be incomplete. These results indicate that ion traps made out of CMOS-compatible materials can perform as well as more traditional traps fabricated from gold with respect to heating and charging as long as methods are developed for controlling oxide growth.

Thesis Supervisor: Isaac L. Chuang
Title: Professor of Physics

Acknowledgments

This document represents not just 18 months of work, but the entirety of my undergraduate experience at MIT. Like any great achievement, it could not have been accomplished without the help of countless people along the way. It is impossible to list all of them; however, several people stand out for their efforts.

I would like to thank the entire Quanta research group for teaching me how to be a better scientist. First and foremost, I would like to thank Professor Isaac Chuang, my thesis advisor. He has given me countless opportunities to challenge myself, and working with him has been an incredible experience. I have endless admiration for his thoughtful insights, patience, and dedication to higher standards. Shannon Wang has been a supportive and patient mentor, and is responsible for my entire knowledge of experimental atomic physics. Yufei Ge deserves thanks for teaching me the art of microfabrication, and Peter Herskind and Tony Kim have always provided me with useful insights.

It said that most of what you learn in college is outside of the classroom. It turns out, there is even a lot to learn outside of the laboratory. I would like to thank Kendra Pugh, Cody Daniel, and Rachel Martin for being there for many of these lessons, and providing sanity and perspective through even the toughest times.

Finally, my family deserves thanks. They have provided all of the support I could ever want, and taught me that the only standards I must meet are my own. There is no appropriate thanks for all that they have done for me.

Contents

List of Figures

Chapter 1

Introduction

1.1 Background

In recent years high-precision atomic physics experiments have found many uses, making ion traps an extremely important technology. Atomic clocks have been created from trapped Al^+ and Be^+ ions with 17 digits of precision[RHS+08], and quantum information science has opened up the possibility of solving computationally intractable problems using precision control of quantum systems [Fey82]. Arrays of ion traps have been proposed as a possible architecture for scalable quantum computing [CZ95], which would allow the speedup of many important and useful algorithms for problems such as solving linear systems [Ara09] and factoring large numbers [Sho97].

An often overlooked fact of trapped ions is that the precise control over the atomic state and its interactions allows for them to be used to make exceedingly precise measurements of thermal fluctuations, surface properties, and other quantum properties of solids. Using the trapped ion as a probe, the fundamental processes behind observed macroscopic phenomena can be examined to extremely high precision. By using the electronic and motional states of a trapped ion to probe the electric field, fluctuations on the order of 10^{-19} V^2 cm^{-2} Hz^{-1} can be detected with a trapped ion located at distances which are tens to hundreds of microns from the metallic surface. These measurements can in turn be correlated to various surface properties of solids, including grain size, structure, composition, and texture. In addition, the electric

field noise can be measured to this level at unprecedentedly high frequencies – previous measurements of this precision could only be achieved at low frequencies (on the order of single Hertz) [DH81][Ray02].

This thesis presents the application of ion traps to studying two such phenomena: electric field noise and the effect of surface physics on the metallic work function. Applications of the suppression of electric field noise and charging of metallic surfaces has found applications in many scientific fields. These physical phenomena are related to the heating of the motional modes in trapped ions and the perturbing of the trapping potential due to trapped surface charges, making the study of such phenomena an important obstacle to surpass in quantum information science [DOS+06]. Electric field noise due to fluctuating surface potentials has been determined to be one of the least understood and highest risk noise sources in the LIGO/LISA Scientific Collaboration, placing a limit on precision measurements of gravitational waves[RBB+06]. Tests of quantum electrodynamics measuring the Casimir-Polder force require measurements on the order of 10^{-11} V m^{-1}, making electric field noise an increasingly important consideration in this field [SBC+93].

Past experiments have successfully determined both the distance and temperature dependence of anomalous noise (noise in excess of the Johnson and shot noise) at high (> 150 K) [DOS+06] and cryogenic [LGA+08][LGL+08] temperatures with tungsten, silver, and gold traps. Similarly, the effects of electrode charging on trap parameters has been studied before in gold electrode multipole traps [MDW08]. However, very few studies have been performed that made comparisons between different electrode materials. Gold has become standard for ion trap electrodes given its high electrical conductivity and resistance to oxidation, but is incompatible with current CMOS fabrication technology. CMOS-compatible metals such as aluminum and copper have been proposed as potential electrode materials to allow for integration with CMOS control electronics to improve scalability of ion traps. This thesis explores the effects that electrode choice has on the performance of ion traps, as characterized by electric field noise and electrode charging. In particular, ion traps are microfabricated with aluminum, copper, and gold as electrode materials, including a set of traps with

additional oxide layers on them to measure the performance of oxidized traps. The majority of original work in this thesis is the development of fabrication methods for these traps, resulting in a procedure that takes 12-15 man-hours (typically spread over the course of a few days) to manufacture a cryogenic surface electrode trap from raw materials. The electric field noise and electrode charging rates are then measured for each trap as a measure of its performance; the goal is to find materials that are CMOS-compatible yet maintain the performance of gold electrode traps.

This thesis is not considered a comprehensive work by any stretch of the imagination. This document focuses on the fabrication and characterization of several series of ion traps; therefore this work does not seek exhaustively characterize the electric field fluctuations. No systematic measurements are made of the temperature or frequency dependence of electric field noise, and the measurements of electrode charging are by no means exhaustive. As a result, no attempt is made at the formulation of a comprehensive model that explains the experimental results. However, this work serves as a starting point for any of these endeavors, laying down the groundwork such that they can be achieved in the future.

1.2 Overview

The scope of this manuscript is twofold. First, the properties of bulk materials are probed using trapped ions as a high-precision instrument for taking data. In addition to measuring the absolute values of these properties, the goal is to fully characterize their dependencies and trends. Second, the goal is to look at these results from a device fabrication standpoint, and to determine which materials are good candidates for use towards scalable quantum information. Throughout this entire thesis, the results of these experiments will be examined through both the physics standpoint and the device standpoint.

Chapter 2 presents the theory of how to trap ions using an oscillating electric field. In this chapter the geometry of the planar Paul Trap is introduced, as are methods by which the stable equilibrium in the field and the motion of the ion can

be modeled. This concludes the theoretical background for this work.

Chapter 3 details the electronic structure of strontium, the atom of choice in this experiment. The electronic and motional structure of strontium is presented, along with methods for coherently manipulating these states. Methods for the detection, cooling, and measurement of strontium ions are presented, providing a way to measure electric field fluctuations in the electrode surface.

Chapter 4 introduces the reader to the theory behind fluctuations in the electric field due to noise and electrode charging. The first half of this chapter derives the spectral densities of the common types of noise in solids, and explains how such noise can be measured in ion traps. The second half begins with an explanation of photoemission in metal-oxide systems, and presents a method for measuring the light-induced electrode charging.

Chapter 5 describes microfabrication techniques used for manufacturing planar ion traps. The entire process is summarized from freshly cut quartz wafers to the packaging of the final trap. In addition, alternative fabrication approaches are discussed, as are modifications to the trap morphology, such as annealing and the thickening of the oxide layer.

Chapter 6 presents experimental results. Using the apparatus described in Chapter 5 and the theory in Chapters 2 and 3, the details of measurements of photoemission and anomalous noise in various materials is presented. In addition, the results of the experiment are compared with the ones predicted by theory in Chapter 2.

Chapter 7 concludes with a discussion of our experimental results, and an outlook on future experiments in this field.

1.3 Contributions

The work described in this document was performed in Professor Isaac Chuang's laboratory at the MIT-Harvard Center of Ultracold Atoms and Research Laboratory for Electronics. Jaroslaw Labaziewicz and Kenneth Brown, former students in the laboratory, led the construction of the apparatus used to take the measurements in

this thesis. Shannon Wang and Yufei Ge oversaw my work directly, which consisted of the fabrication of the ion traps in this thesis. The measurements were performed by Shannon Wang, assisted by Peter Herskind and Jeffrey Russom. Yufei Ge oversaw my work in fabrication, both teaching and assisting me in the process of manufacturing ion traps.

Chapter 2

Ion Trapping

In this chapter, the theory of ion dynamics in a linear Paul trap is presented. The chapter begins with motivation for the Paul trap, followed by the full solution to atomic motion in the potential field using the Mathieu Equation and Floquet Theory. The Secular Approximation is then introduced to reformulate the equations of motion into a form that proves to be much more intuitive. The chapter closes with the introduction of the surface electrode geometry, and how the theory built up for the linear quadrupole trap can be applied to it.

2.1 Linear Quadrupole Traps

A static electric field cannot trap an ion, as dictated by Earnshaw's Theorem [Ear42]. Any minimum in a potential can be expanded as a harmonic potential $V(x, y, z) = \alpha x^2 + \beta y^2 + \gamma z^2$ for small displacements. By Laplace's Theorem ($\nabla^2 V(x, y, z) = 0$), we find that $\alpha+\beta+\gamma = 0$ – there is no purely attractive or purely repulsive minimum.

It wasn't until the discoveries by Penning (using magnetic fields) and Paul (using oscillating electric fields) that a method for creating a trapping potential was formulated [PS53] [Pau90]. Paul's method used electric fields oscillating a radio frequencies to create a quadrupole potential; the original trap has been modified several times for ease of production, with one of the simpler Paul traps shown in Figure 2-1. This trap (called the linear quadrupole trap) has four rods; two of them are grounded

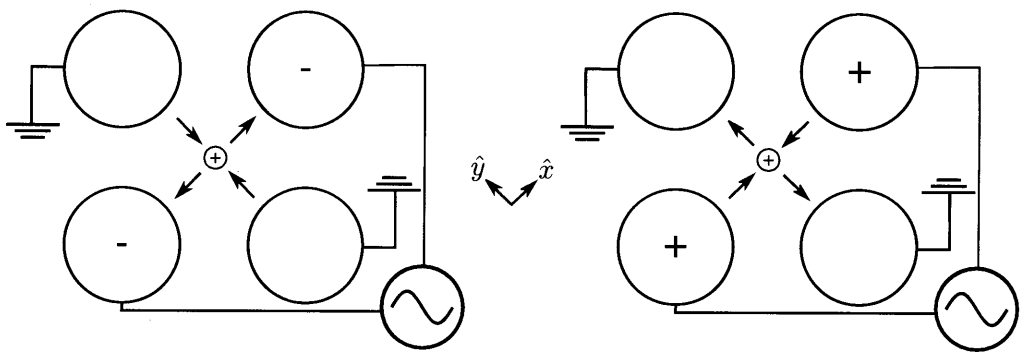

Figure 2-1: Demonstration of how the oscillating potentials in a linear quadrupole trap can trap a positively charge particle.

and the remaining two hold a voltage that oscillates at radio frequencies. The entire line down the center of the four rod configuration is a stable equilibrium; however, positive static voltages are needed at the ends to prevent the trapped particles from leaking out axially.

2.2 The Mathieu Equation

The most general time-independent quadrupole potential takes the form of:

$$\phi = \alpha x^2 + \beta y^2 \tag{2.1}$$

By Laplace's Theorem, we find that $\alpha = -\beta$; the potential must be attractive in one direction and repulsive in the other direction, as shown in Figure 2-2. If the potential oscillates at a high enough frequency, an ion can be trapped in the center of the potential.

The full time-dependent potential is given in Equation 2.2, such that V_0 is a DC bias, V_1 is the amplitude of the radio frequency potential, r_0 is the distance from the center of the quadrupole to the conducting rods, and Ω is the frequency of oscillation.

$$\phi(x, y, t) = \frac{x^2 - y^2}{2r_0^2}(V_0 - V_1 \cos \Omega t) \tag{2.2}$$

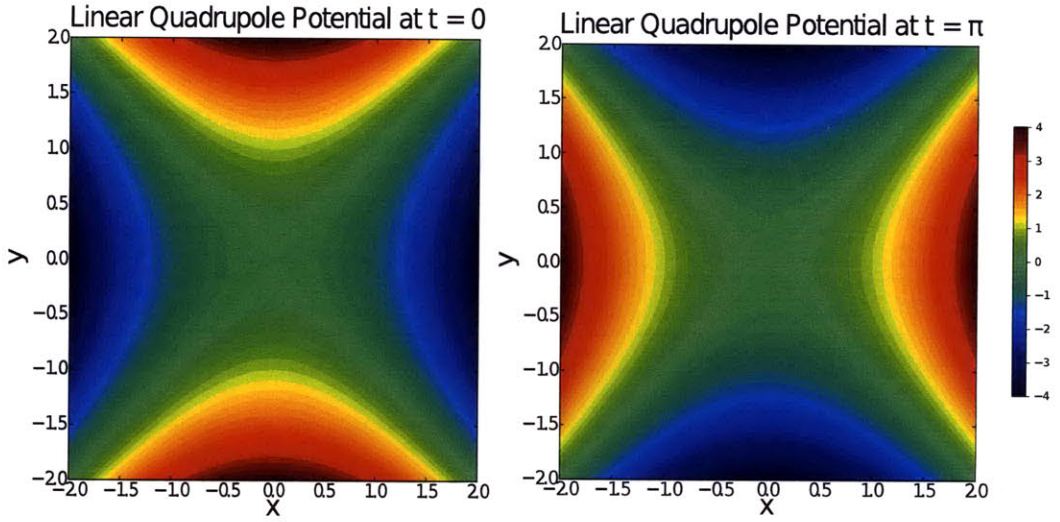

Figure 2-2: Equipotential Surfaces of the linear quadrupole trap for times $t = 0$ and $t = \pi$.

We can solve for the equations of motion in the $\hat{x}$- and $\hat{y}$-directions separately; due to symmetry we can assume that the solutions in the $\hat{x}$- and $\hat{y}$-directions are related by a factor of -1. We solve for the equation of motion using

$$m\ddot{x} = -Q\nabla\phi(x,t) \tag{2.3}$$

Here, Q and m are the charge and mass of the particle and $\phi(x,t)$ is the potential with the y-component set to zero. Plugging in the potential:

$$\ddot{x} + Q\left(\frac{V_0 + V_1\cos\Omega t}{mr_0^2}\right)x = 0 \tag{2.4}$$

Making the equation dimensionless, it takes the form of the canonical Mathieu Equation[1] [Mat68]:

$$\frac{d^2x}{d\xi^2} + (a - 2q\cos(2\xi))x = 0 \tag{2.5}$$

With dimensionless Mathieu parameters

[1]If this equation was solved for y rather than x, the substitutions $x = y$, $a = -a$, $q = -q$ would be made.

$$q = \frac{2QV_1}{m\Omega^2 r_0^2} \tag{2.6}$$

$$a = \frac{4QV_0}{m\Omega^2 r_0^2} \tag{2.7}$$

$$\xi = \frac{\Omega t}{2} \tag{2.8}$$

Here, a is the dimensionless DC voltage, q is the dimensionless RF voltage, and ξ is the dimensionless time. The solutions to this equation are well-known; using Floquet Theory we find that the solutions take the form [Flo83]:

$$x(\xi) = c_0 e^{\lambda\xi}\varphi(\xi) + c_1 e^{-\lambda\xi}\varphi(-\xi) \tag{2.9}$$

with integration constants c_1 and c_2. In Floquet's solution, $\varphi(\xi)$ is a function that is periodic in ξ, and λ is a characteristic exponent dependent upon the particular values of a and q. This solution can be simplified further using Fourier's Theorem to expand $\varphi(\xi)$:

$$x(\xi) = c_0 e^{\lambda\xi} \sum_{n=-\infty}^{\infty} c_{2n} e^{2in\xi} + c_1 e^{-\lambda\xi} \sum_{n=-\infty}^{\infty} c_{2n} e^{-2in\xi} \tag{2.10}$$

Making the simplification $\lambda = \gamma + i\delta$ and absorbing the real part into the integration constants:

$$x(\xi) = c_0' \sum_{n=-\infty}^{\infty} c_{2n} e^{i(2n-\delta)\xi} + c_1' \sum_{n=-\infty}^{\infty} c_{2n} e^{-i(2n-\delta)\xi} \tag{2.11}$$

Using Euler's Relation[2] to simplify this further:

$$x(\xi) = (c_0' + c_1') \sum_{n=-\infty}^{\infty} c_{2n} \cos\left((2n-\delta)\xi\right) + i(c_0' - c_1') \sum_{n=-\infty}^{\infty} c_{2n} \sin\left((2n-\delta)\xi\right) \tag{2.12}$$

These functions are called Mathieu functions of integral order [Mac47]. This

[2] $e^{i\theta} = \cos\theta + i\sin\theta$

simplification highlights how the stability of solutions is dependent upon the value of δ – if δ is an integer value, then the solutions are unstable; if it is non-integer valued, then our solutions are stable. Thus, the stability is purely a function of a and q. There should exist regions of the a-q parameter space for which stable solutions exist, and other areas for which the solutions are unstable. In the case of no DC voltages ($V_0 = 0$), it can be shown that the maximum stable q is 0.908 [Mac47]. In other words:

$$\frac{2QV_1}{mr_0^2\Omega^2} < 0.908 \tag{2.13}$$

Therefore, the stability of the trapped ion can be entirely determined by the free parameters V_1 and Ω – the amplitude and frequency of our AC potential.

2.3 The Secular Approximation

The Floquet solution to the Mathieu Equation fully describes the motion of atoms in a quadrupole potential, though it provides very little intuition about ion dynamics. By applying an appropriate approximation, the solutions take a much more intuitive form – this approximation is called the Secular Approximation.

Depending on the chosen time scale, an ion trapped in a potential field oscillating at frequency Ω experiences two qualitatively different phenomena. For time scales on the order of Ω^{-1}, the ion experiences a force proportional to $\sin \Omega t$. Treating this as a driven oscillator, the ion will oscillate with a drive frequency Ω with a small amplitude (also proportional to the drive frequency). This motion is called the micromotion of the ion. For time scales such that $t \gg \Omega^{-1}$, the ion will see a time-averaged potential field; therefore the ion effectively experiences a two-dimensional harmonic potential. An ion in this potential will undergo simple harmonic motion at a frequency ω, which we will define as the secular frequency, ω_{sec}. The total motion of the ion can be approximated as a superposition of these two modes.

Referring back to Equation 2.4, we can write the two-dimensional equations of motion as:

$$\begin{bmatrix} \ddot{x} \\ \ddot{y} \end{bmatrix} = \frac{QV_1}{mr_0^2} \cos(\Omega t) \begin{bmatrix} -x \\ y \end{bmatrix} \tag{2.14}$$

In the Secular Approximation, it is assumed that the secular motion is much larger than the micromotion ($x_{sec} \gg x_\mu$) and that the drive frequency governs the acceleration in the potential ($\ddot{x}_\mu \gg \ddot{x}_{sec}$) [Kap51][Ric06]. Assuming the Secular Approximation and no DC voltages, the equations of motion become:

$$\begin{bmatrix} \ddot{x}_\mu \\ \ddot{y}_\mu \end{bmatrix} = \frac{QV_1}{mr_0^2} \cos(\Omega t) \begin{bmatrix} -x_{sec} \\ y_{sec} \end{bmatrix} \tag{2.15}$$

Integrating twice, the equation for micromotion becomes:

$$\begin{bmatrix} x_\mu \\ y_\mu \end{bmatrix} = \frac{QV_1}{mr_0^2\Omega^2} \cos(\Omega t) \begin{bmatrix} x_{sec} \\ -y_{sec} \end{bmatrix} \tag{2.16}$$

As predicted, the micromotion oscillates about the secular motion with a frequency Ω. Rewriting the prefactor as $q/2$, where q is the Mathieu parameter, the restriction that $x_\mu < 0.454 x_{sec}$ is enforced – the micromotion's amplitude must be smaller than that of the secular motion. Using Equations 2.15 and 2.16, the secular motion can be solved for:

$$\begin{bmatrix} \ddot{x}_{sec} \\ \ddot{y}_{sec} \end{bmatrix} = -\frac{Q^2V_1^2}{m^2r_0^4} \cos^2(\Omega t) \begin{bmatrix} -x_{sec} \\ y_{sec} \end{bmatrix} \tag{2.17}$$

The secular potential is essentially a time-averaged one (looking at the potential over large time scales such that it becomes harmonic). Time-averaging the cosine term ($\langle \cos^2(\Omega t) \rangle = 1/2$):

$$\begin{bmatrix} \ddot{x}_{sec} \\ \ddot{y}_{sec} \end{bmatrix} = -\frac{Q^2V_1^2}{2m^2r_0^4} \begin{bmatrix} -x_{sec} \\ y_{sec} \end{bmatrix} \tag{2.18}$$

The secular motion can now be found easily by integration. The secular motion in the potential becomes:

$$x = c_0 \cos(\omega_{sec} t + \Phi_0) \tag{2.19}$$

$$y = c_1 \cos(\omega_{sec} t + \Phi_1) \tag{2.20}$$

such that c_0 and c_1 are integration constants and Φ_0 and Φ_1 are phase factors. The secular frequency is given by:

$$\omega_{sec} = \frac{QV_1}{\sqrt{2} m r_0^2 \Omega} \tag{2.21}$$

Having found the secular frequency, the pseudopotential of the trap can be written as

$$V(x) = \frac{1}{2} m \omega_{sec}^2 (x^2 + y^2) = \left(\frac{Q^2 V_1^2}{4 m r_0^4 \Omega} \right)^2 (x^2 + y^2) \tag{2.22}$$

giving the full pseudopotential.

2.4 Surface Electrode Traps

In 2005, Chiaverini *et al.* proposed a surface electrode version of the linear quadrupole trap, shown in Figure 2-3 [CBB+05]. In this planar trap, all of the electrodes lie in a single plane and the ion is trapped above the surface, opening up the possibility of using microfabrication techniques for production of these surface electrode traps. The techniques used are explained in depth in Chapter 4. The surface electrode Paul trap is used in the rest of this thesis.

While the surface electrode geometry is conceptually similar to the linear Paul trap geometry (as shown in Figure 2-3), the mathematics are significantly more difficult to solve analytically. The pseudopotential approximation still holds (the approximation was made independent of geometry), but the analytic forms of the trap parameters are now altered. For a surface electrode trap with dimensions as given in Figure 2-4, the analytic form of the potential in the xz plane is given by [Hou08]:

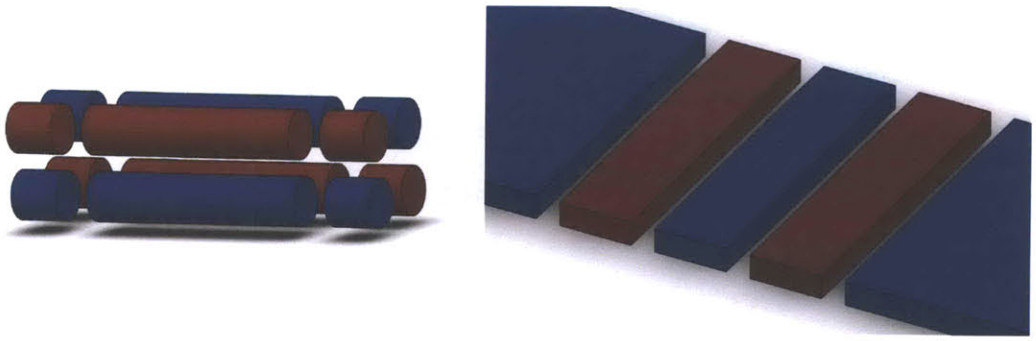

Figure 2-3: A linear quadrupole trap (left) and a planar Paul trap (right). Red indicates ground and blue indicates oscillating voltages. Note how the linear quadrupole trap can be "unfolded" into the planar trap by orientating the electrodes in a plane rather than a cylinder.

$$\Phi(x,z,t) = \frac{V_1}{\pi}\left[\tan^{-1}(\frac{a+b-x}{z}) - \tan^{-1}(\frac{a-x}{z}) - \tan^{-1}(\frac{x}{z}) + \tan^{-1}(\frac{c+x}{z})\right]\cos\Omega t \tag{2.23}$$

For the surface electrode design, the Mathieu parameter q becomes a matrix with elements

$$q_{11} = -q_{22} = \frac{-4QV_1}{\pi m\Omega^2}\frac{a^2(b^2-6bc+c^2)+a(b+c)(b^2-6bc+c^2)-bc(b+c)^2}{(a+b)^2(a+c)^2\sqrt{abc(a+b+c)}} \tag{2.24}$$

$$q_{12} = q_{21} = \frac{8QV_1}{\pi m\Omega^2}\frac{(b-c)(2a+b+c)}{(a+b)^2(a+c)^2} \tag{2.25}$$

The stability of the trap can then be computed using this Mathieu parameter.

An important concept for the operation of surface electrode traps is that of compensation. The geometry of the trap creates a nodal line down the axis of the center electrodes. Nonzero micromotion amplitudes due to trap defects and stray fields make it difficult to hold the trapped ion in the center of the potential; in addition, increased micromotion may cause Doppler shifts in atomic transitions, making it highly undesirable [BMB+98]. By applying DC voltages to the outer electrodes, the trapped ion can be pushed back into the center of the well, eliminating its micromotion.

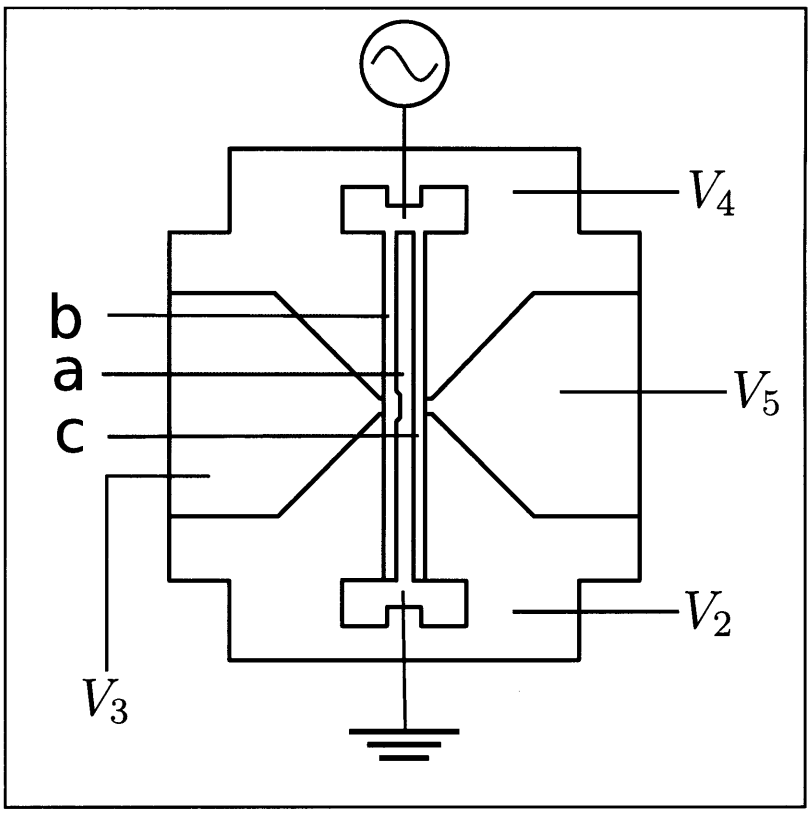

Figure 2-4: The geometry of the surface electrode traps used in this thesis. "a", "b", and "c" indicate the widths of the radio frequency driven electrodes and the ground electrodes. The four remaining electrodes (V_2 through V_5) surrounding the central ones are held at DC voltages used for compensation. The entire trap is typically 1 cm $\times$ 1 cm, with a typical electrode width of 150 μm.

One of the disadvantages of the surface electrode design is that it restricts optical access to a hemisphere. Therefore, laser access is constrained to be in only the plane of the trap. For laser cooling, the laser must have a non-zero projection onto the axis to be cooled – the radial mode cannot be cooled with this scheme. This problem is resolved by introducing asymmetry to the trap design, tilting the radial mode slightly such that it has a nonzero axial component (see Figure 2-4).

2.5 Summary

This chapter described the theoretical foundations of ion dynamics within a linear Paul trap (and, by extension, a planar Paul trap). Starting from an oscillating linear

quadrupole potential, the equations of motion were solved in their exact form using Floquet Theory and the Mathieu Equation. Next, the Secular Approximation was introduced to provide a more intuitive view of ion dynamics. Using this model, the secular potential was derived and along with it the two components of the ion's motion – the secular motion and the micromotion. Section 2.4 discusses the transition from a three-dimensional quadrupole trap to a planar surface electrode trap, and how the change in geometry influences the relevant trapping parameters. The theory that we have developed here will be revisited in later chapters when experimentally trapping ions is discussed.

Chapter 3

The $^{88}Sr^{+}$ Ion

All experiments in this thesis utilize the $^{88}Sr^{+}$ ion as the trapped species. The singly-ionized species has no nuclear spin and a single valence electron, giving it a very simple hydrogenic energy structure. All of the relevant transitions (shown in Figure 3-1) are available as diode lasers, reducing the cost and complexity of the laser systems used to coherently manipulate the ion. In addition, all of the relevant transitions are also within the transparency spectrum of common optical glasses and optical fibers, allowing for easy integration of optics. Our desired isotope, the ^{88}Sr isotope, is the most abundant isotope (83% abundancy), removing the need for an isotopically selective ion source. From a quantum information standpoint, the long lifetime (390 ms) of the $5S_{1/2} \rightarrow 4D_{5/2}$ transition makes it an compelling candidate for information storage. For these reasons, $^{88}Sr^{+}$ is an appealing candidate for a trapped ion. This chapter describes the energy structure of the $^{88}Sr^{+}$ ion and how basic operations (detection, state preparation, and state measurement) are performed on the trapped ion.

3.1 Detection

The first step is to detect the ion and then prepare it into a known energy state. The 422 nm transition is used for both detection and cooling of the ion. When irradiated with 422 nm light, the strontium ion will absorb the photon and its single electron will become excited from the $5S_{1/2}$ state to the $5P_{1/2}$ state (See Figure 3-1). The

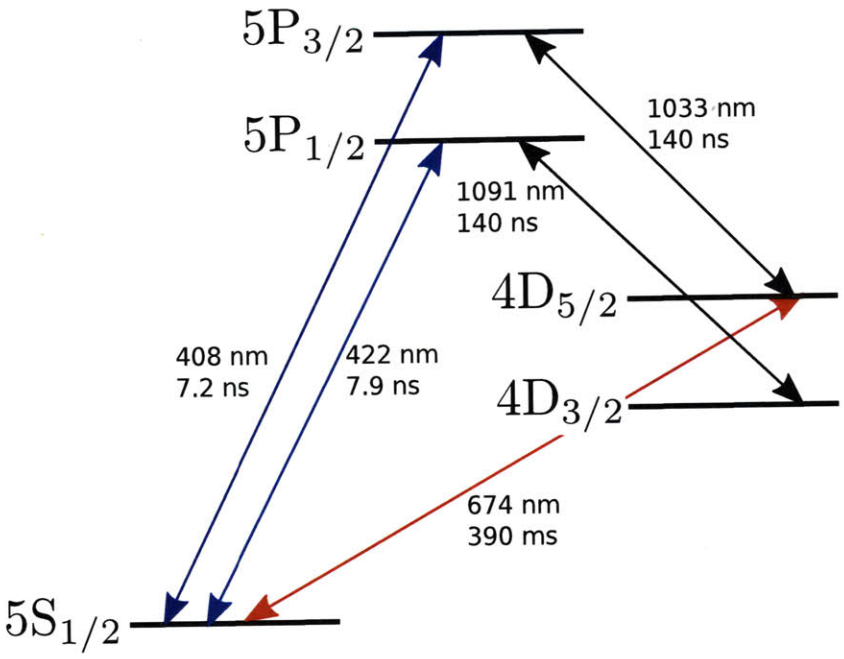

Figure 3-1: The relevant electronic structure of the $^{88}Sr^{+}$ ion. All transitions are labeled with their wavelengths in air and the lifetimes of the transitions.

electron will then decay back into the ground state and emit a 422 nm photon in a random direction after 7.9 ns (the lifetime of the transition) on average. This provides a straightforward method for detection – the $5S_{1/2} \rightarrow 5P_{1/2}$ transition can be used to induce fluorescence of the ion, and the emitted photons can be detected to determine if an ion has been trapped.

Once the ion is detected within the trap, the next step is to prepare the ion into a known motional state. A trapped ion begins in a completely unknown motional state, and therefore the ion must be cooled to its ground state before any experiments can be performed. This is accomplished through two processes – Doppler cooling and sideband cooling.

3.2 Doppler Cooling

The Doppler cooling process uses the $5S_{1/2} \rightarrow 5P_{1/2}$ transition to cool the trapped ion. By tuning the 422 nm laser off-resonance to the red, atoms can be selectively targeted. The vibrating atom will see a Doppler-shifted frequency for the incident light; only atoms that are moving towards the laser will see resonant light. Upon absorption of the resonant photon, the atom is imparted momentum $\hbar k$ in the opposite direction to its motion. The atom subsequently emits a 422 nm photon in a random direction, and experiences a recoil of $\hbar k$ in the direction opposite to the emission. Averaged over multiple absorptions and emissions, the emission recoil is negligible, so the atom loses a net momentum of $\hbar k$ per scattering event. Through repeated iterations with a decreasing frequency shift, the total energy of the atom can be decreased.

The cooling process can be interrupted by the $5P_{1/2} \rightarrow 4D_{3/2}$ transition. With 1/14 probability, the $5P_{1/2}$ state will decay to the $4D_{3/2}$ state instead of the $5S_{1/2}$ state. The $4D_{3/2}$ state is metastable and has a lifetime approximately 5×10^7 longer than that of the $5P_{1/2}$ state and prevents further cooling. The addition of a 1091 nm laser allows the atom to be re-excited into the $5P_{1/2}$ state such that the cooling process can continue.

The nonzero recoil with each emitted photon imposes a limit on how much the atom can be cooled. Each emission heats the atom back up, creating a temperature limit of $T = \frac{\hbar\Gamma}{2k_B}$, where Γ is the linewidth of the atomic transition and k_B is Boltzmann's constant [YCD89]. Assuming Doppler cooling in all three directions using the 422 nm transition, the Doppler limit is $T = 76\mu$K. This is not sufficient to cool the ion to the ground state, so different cooling methods must be utilized in order to achieve a controlled state.

3.3 Sideband Cooling

In order to cool below the Doppler Limit, the full energy structure of the trapped ion, shown in Figure 3-2, must be used. Chapter 2 derived the external potential

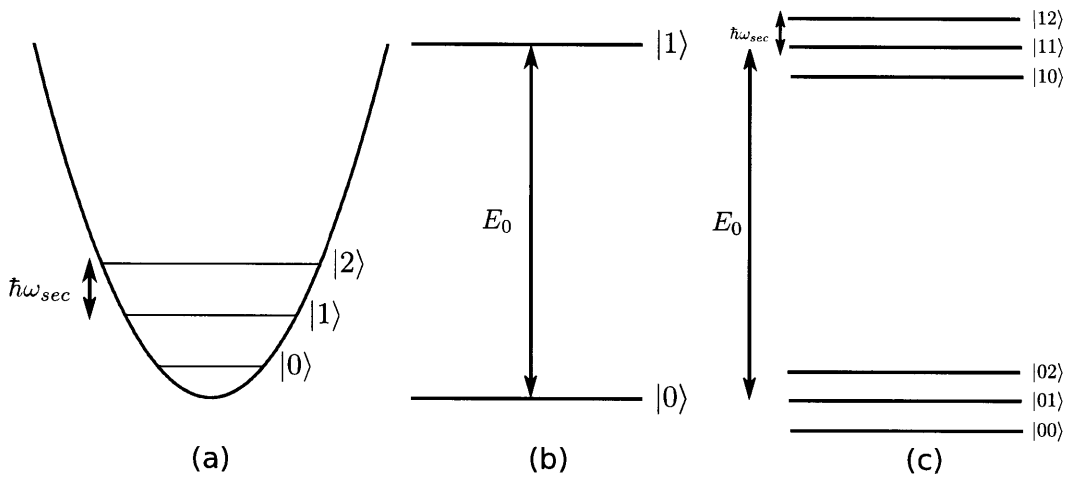

Figure 3-2: (a) The energy spectrum of a trapped ion in a harmonic oscillator with frequency $\hbar\omega_{sec}$ (b) The electronic structure relevant to any transition can be modeled as a two-state system with energy separation E_0 (c) A trapped ion exhibits an overall energy structure that is the coupling of the two separate energy spectra.

that traps the ion in great detail. As described in Chapter 2, the potential can be approximated as a harmonic potential near the trap's center (See Figure 3-2a). The ion vibrates in the potential with quantized motional modes separated by energy $\hbar\omega_{sec}$. Combined with the simple two-state electronic structure of the relevant optical transition (shown in Figures 3-1,3-2b), the overall energy structure of the ion is the product of the two energy spectra as shown in Figure 3-2c.

After Doppler cooling, the ion is cold enough that the thermal broadening of the $5S_{1/2} \rightarrow 4D_{5/2}$ transition is negligible and the motional sidebands can be resolved. This allows what is called sideband cooling. As with Doppler cooling, light that is resonant with the atomic transition will be absorbed by the ion. The coupling of the internal and external states allows many more optical resonances for the ion than are available for Doppler cooling – any light of frequency $\omega_0 \pm n\omega_{sec}$ will be absorbed, where n is an integer. These motional sidebands can be used to precisely control the motional state of the ion using optical interactions.

An ion that is in the electronic ground state and mth motional mode ($|5S_{1/2}, m\rangle$) can be excited to the $|4D_{5/2}, m-1\rangle$ state by an off-resonance laser pulse with frequency

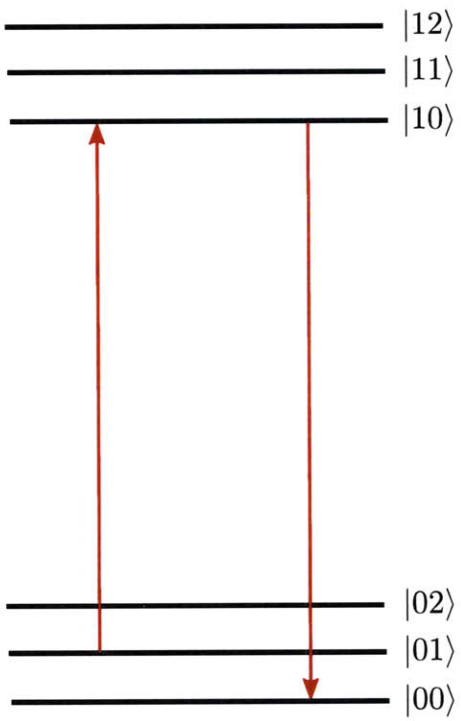

Figure 3-3: Sideband cooling

$\omega_{S\to D} - \omega_{sec}$. The $4D_{5/2}$ state has a long lifetime, so the 1033 nm laser is used to pump the ion into the rapidly decaying $5P_{3/2}$ state, which will spontaneously decay into the $|5S_{1/2}, m\rangle$, $|5S_{1/2}, m-1\rangle$, or $|5S_{1/2}, m-2\rangle$ state with equal probability. Thus a full cycle results in the loss of, on average, a single motional quanta. This process can be iterated as many times as necessary to reach the $|5S_{1/2}, 0\rangle$ ground state, which is realized when the lower (red) sideband (the $\omega_0 - \omega_{sec}$ resonance) disappears because no lower energy motional states are available.

3.4 Measurements

3.4.1 Heating Rate Measurements

The motional sidebands can also be used to precisely measure the rate at which thermal occupation changes, which is linked to anomalous noise in Chapter 4. By

measuring the transition probabilities on the red (lower) and blue (upper) sidebands using appropriately detuned laser pulses, the exact thermal occupation number can be determined.

The trapped ion is first sideband cooled on the $5S_{1/2} \rightarrow 4D_{5/2}$ transition, and then the motional state of the ion is measured via scattering on the $5S_{1/2} \rightarrow 4P_{1/2}$ transition. This is repeated many times (on the order of 100) to determine a transition amplitude for the blue and red sidebands. The thermal occupation number can then be determined as a ratio of the transition amplitudes [WIBH87]:

$$\frac{A_{blue}}{A_{red}} = \frac{\langle n \rangle + 1}{\langle n \rangle} \tag{3.1}$$

Rearranging terms, $\langle n \rangle$ is given by:

$$\langle n \rangle = \frac{A_{red}}{A_{blue} - A_{red}} \tag{3.2}$$

Thus the thermal occupation number can be determined coherently by simply measuring the ratio of the blue and red sideband transition amplitudes. This allows highly accurate measurements of the occupation number to be made without disturbing the trapped ion. The heating rate $\langle \dot{n} \rangle$ is determined by stopping the cooling process for a known amount of time t_0 and then measuring the thermal occupation number at a time $t_0 + \Delta t$. Thus the heating rate is given by:

$$\langle \dot{n} \rangle = \frac{\langle n(t_0 + \Delta t) \rangle - \langle n(t_0) \rangle}{\Delta t} \tag{3.3}$$

3.4.2 Micromotion Measurements

The micromotion amplitude of a trapped ion can be measured using the "cross-correlation" technique [BMB+98]. This method detects the excess micromotion by observing the change in the atom's fluorescence due the first-order Doppler shift induced by the oscillations. The micromotion oscillates at the drive frequency Ω about the secular motion; by observing photons at the drive frequency, the amplitude of the micromotion can be determined. The DC voltages can then be manipulated

until the micromotion amplitude goes to zero and the ion is fully compensated.

3.5 Summary

This chapter detailed the electronic and motional structure of the strontium ion and how this energy structure can be used to perform high-precision experiments. The theory of cooling ions to their motional ground state was explained, and then a method for measuring the change in thermal occupation number was presented. Now that the ability to make precision measurements of the heating rate of trapped strontium ions has been presented, the next chapter explores the cause of these heating rates.

Chapter 4

Anomalous Noise and Light-Induced Charging

For scalable quantum computation to be realized, the qubit candidate must have extremely long lifetimes for the proposed qubit. For $^{88}Sr^{+}$, the $5S_{1/2} \rightarrow 4D_{5/2}$ transition has been offered as an appealing candidate for a electronic qubit, with its motional state as a qubit. In practice, the motional qubit is highly susceptible to heating out of the ground state from a variety of sources, including collisions with background gas and noise in the trapping potential. In a vacuum environment, the primary source of heating of the motional mode is due to electric field noise from nearby electrodes.

Electric field noise has many proposed causes, such as changing grain sizes in the bulk [GGJM+06], adsorbates introducing new surface energy states [RO92], and charge traps creating excess surface charging [OCK+06]. Fluctuations in any of these parameters could potentially change the local charge on the surface or scatter conducting electrons, perturbing the electric field as seen by the ion. In addition, these parameters should exhibit some material-dependence. This chapter introduces the theory of noise in solids, and then introduces how the noise can be coupled to the motional modes of the trapped ion.

In addition, the use of optical interactions to coherently manipulate trapped ions poses a problem as ion traps are scaled down. As the ion is held closer and closer to the electrode surface, the surface physics become much more significant. In particular,

charging of the surface electrodes due to photoemission of electrons can disturb the trapping potential. This chapter elaborates on the relevant surface physics and how such charging of the surface electrodes can be measured.

4.1 Noise in Solids

4.1.1 Introduction to Noise

In electronic circuits, noise is a random fluctuation in the electrical signal (either voltage or current) with time. Given a quantity $\lambda(t)$ that fluctuates with time, it is common to describe the noise in the frequency domain rather than the time domain; this is known as the power spectrum or power spectral density:

$$S(\omega) = |\Lambda(\omega)|^2 \tag{4.1}$$

such that $\Lambda(\omega)$ is the Fourier transform of the time-domain quantity $\lambda(t)$, given by

$$\Lambda(\omega) = \int_{-\infty}^{\infty} \lambda(t) e^{-i\omega t} dt \tag{4.2}$$

For noise that is a time-independent fluctuating quantity (such as Johnson noise or shot noise), the power spectrum is frequency-independent. Figure 4-1 shows a cosine function with noise and the associated power spectrum. The noise is fairly flat for all frequencies, and exhibits no power law-like behavior.

The power spectrum acquires a frequency dependence when the fluctuating variable can be associated with a finite relaxation time, $\pi(t)$. Assuming a relaxation function of the form $\pi(t) \propto e^{-t/\tau}$ with a constant relaxation time τ, it can be shown that the power spectral density takes the Lorentzian form[Ray02]:

$$S(\omega) \propto \frac{2\tau}{1 + (f\tau)^2} \tag{4.3}$$

For low frequencies ($f \ll \tau^{-1}$), $S(\omega)$ shows a white power spectrum, independent of the frequency. As the frequency increases past $f = \tau^{-1}$, the noise begins to exhibit

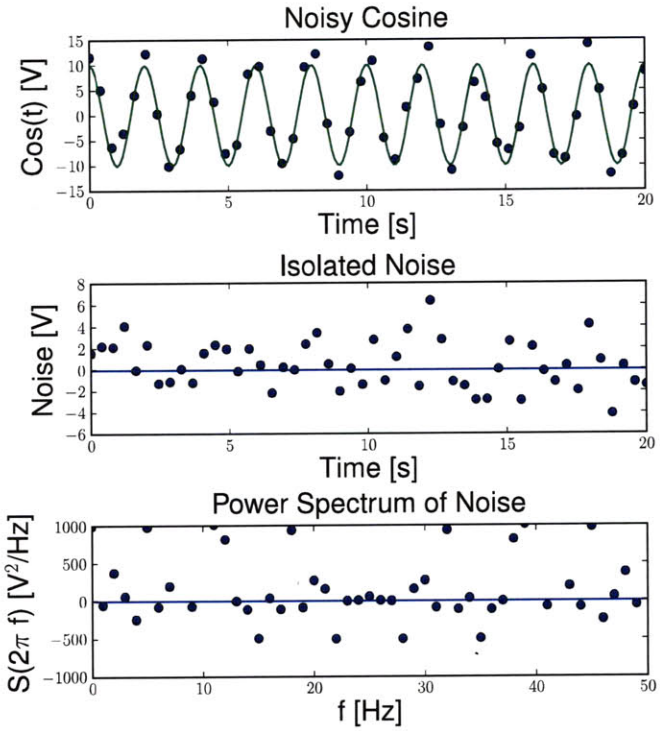

Figure 4-1: Top: A cosine voltage source with randomly generated noise added. Middle: The isolated noise from the circuit. Bottom: The power spectrum of the noisy cosine function. Note that the power spectrum is independent of frequency, implying a random source of noise.

a f^{-2}-type form.

Assuming that there exist a variety of relaxation phenomena that are correlated to the noise, with a distribution of relaxation times τ, the power spectrum can be described by:

$$S(\omega) \propto \int_0^\infty d\tau F(\tau) \frac{2\tau}{1+(f\tau)^2} \tag{4.4}$$

such that $F(\tau)$ represents the distribution of relaxation times.

Figure 4-2 demonstrates how a distribution of relaxation phenomena can give rise to a 1/f-type noise. Similarly, specific distributions of noise can give rise to inverse power law-type noise. In general, it has been observed that a distribution of the form $\tau^{-\alpha}$ gives rise to a $f^{-2+\alpha}$-type power spectra.

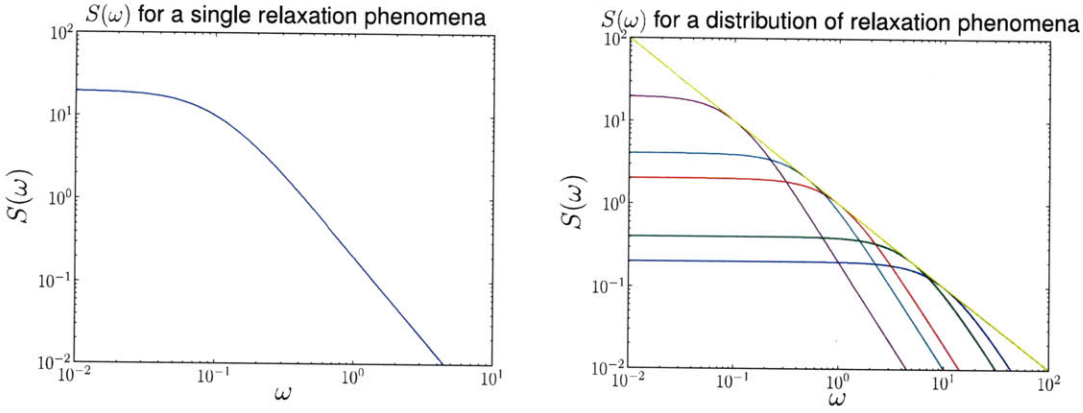

Figure 4-2: Left: The power spectrum of a variable whose fluctuations are associated with a single relaxation phenomena. Right: The power spectrum of a variable whose fluctuations are associated with multiple relaxation phenomena. Here, it is demonstrated how a variety of relaxation phenomena could lead to 1/f-type spectra (shown in yellow).

Another useful measure of the noise is the root mean squared fluctations of the time-dependent value. This gives us the value of averaged value of the fluctations, and is given by:

$$\langle(\delta\lambda(t))^2\rangle = \frac{1}{2\pi}\int_{f_0}^{f_1} S(\omega)df \tag{4.5}$$

where f_0 and f_1 define the limits of the frequency band the measurement is taken in.

4.1.2 Types of noise

Three types of electronic noise are commonly observed in solids: shot noise, Johnson-Nyquist noise, and anomalous (excess) noise.

Shot noise, discovered by Schottky in 1918, is the noise due to the discretization of charge carriers in a conductor [Sch18]. The current in a solid is proportional to nQv, where n is the number of electrons, Q is the electron charge, and v is the velocity of the electrons. Therefore, noise can be observed as fluctations in both n and v. shot noise is the former. The macroscopic current observed is the sum of many electrons each contributing Q towards the total current – the fluctations in n from one moment in time to another is the shot noise. It has the voltage power spectrum

$$S_V(\omega) = 2Q\langle I\rangle R(\omega)^2 \tag{4.6}$$

where $R(\omega)$ is the resistance of the conductor being driven by an oscillating voltage of frequency ω. This power spectrum indicates that the shot noise is both frequency- and temperature-independent. However, shot noise is typically so small that it can only be observed when both Johnson noise and anomalous noise have been suppressed.

Johnson noise, discovered in 1928 by H. Nyquist and J. Johnson, is best described as fluctuations in the velocities of electrons in a conductor [Joh28]. The kinetic energies of electrons in a conductor can be described by the Maxwell-Boltzmann Distribution; therefore there exists a variance of velocities that corresponds to temperature. The power spectrum of Johnson noise is [Nyq28]:

$$S_V(\omega) = 4k_B T R(\omega) \tag{4.7}$$

such that k_B is Boltzmann's Constant, and T is the temperature. The power spectrum indicates that Johnson noise is dependent upon the temperature of the solid, but is not dependent upon any inherent material properties or the frequency. Therefore, this noise is expected to decrease with temperature and be an approximate measure of the electron temperature.

The final type of noise is the excess noise – any noise in excess of the shot and Johnson noise. This is also called anomalous noise. The exact causes of anomalous noise is currently unknown, but many phenomenological models exist to describe the experimental data [DH81] [Wei87]. However, decades of experiment have resulted in many qualitative observations about this type of noise.

Anomalous noise possesses a power spectrum $S(\omega) \propto f^{-\alpha}$, such that α is typically small and negative[1]. In an ion trap, the magnitude of the anomalous noise can only be observed at low frequencies (< 1 KHz) or low temperature such that it is larger than the Johnson noise; in addition, it has been found to be related to some thermally-activated process [LGL+08]. The power-law nature of anomalous noise is most likely

[1]When $\alpha = 1$, the anomalous noise becomes the ubiquitous "1/f noise"

to be a result of a distribution of relaxation phenomena that are related to the bulk material; a greater understanding of this noise would give a clearer picture of what sorts of relaxation phenomena and defect kinetics occur in a solid.

For such a noise that is derived from thermally-activated relaxation phenomena, the materials-dependence is unclear. Without knowing the exact processes which give rise to noise in a particular solid, appropriate scaling laws cannot be developed. However, the general classes of relaxation phenomena should give rise to conductivity fluctuations through scattering, carrier diffusion, and other such kinetic processes. Therefore most materials should exhibit the same relaxation phenomena, but with variations in the activation energies and relaxation times. It is unlikely that there is more than an order of magnitude variation in these parameters, so the materials dependence should be small if it exists.

A complete theory of noise would possess three components [Ray02]:

- A clear identification of the fluctuating value and mechanism
- A coupling between the fluctuating mechanism and electron motion in the solid, leading to conductivity fluctuations
- Appropriate characterization of the fluctuation dynamics such that a relaxation function $\pi(t)$ can be found and the spectral power $S(\omega)$ can be calculated.

Such a theory of noise would make noise spectroscopy an invaluable tool in the characterization of the quality of metallic films. Currently, the models for anomalous noise can be categorized into two classes: phenomenological models and fluctuation models. The first category of models, such as the Dutta-Horn Model, do not deal with specific defects or coupling mechanisms; instead, they attempt to describe the power spectrum of anomalous noise. The Dutta-Horn model is based on a distribution of activation energies for thermally-activated phenomena, such that a $1/f$-type spectrum is obtained. Using the Arrhenius-type equation with activation energy E_a $\tau = \tau_0 e^{-E_a/kt}$ to describe the relaxation time, the spectral power can be written [DH81]:

$$S(\omega) \propto \int_0^{\inf} D(E) \frac{2\tau_0 e^{E_a/k_B T}}{1 + (\omega \tau_0 e^{E_a/k_B T})^2} dE \tag{4.8}$$

with the distribution of activation energies $D(E)$ representing the multiple responsible phenomena. Note that this model makes zero claims about the source of the noise, and only attempts to mathematically describe the functional form of the noise.

The second category of models, such as the Universal Conductance Fluctuation (UCF) or Local Interference model, propose physical processes that could generate fluctuations in the conductivity (such as fluctuations in mobility or the resistivity tensor) [SF86] [JP87]. However, such models do not give a clear mathematical model for the magnitude of these fluctuations, nor do they attempt to characterize the power spectra that such fluctuations would cause.

4.1.3 Electric Field Noise Observed in Ion Trapping

The previous two sections introduced the mathematical language of noise and then the forms of noise in solids. This section represents the culmination of the previous three chapters – how noise can be detected and measured within an ion trap.

Chapter 2 introduced the secular approximation, in which the oscillating electric field can be approximated as a two-dimensional harmonic oscillator with frequency ω_{sec}. The Hamiltonian for such a particle trapped in such a pseudopotential would be

$$H_0 = \frac{\vec{p}^2}{2m} + \frac{m\omega_{sec}^2 \vec{x}^2}{2} \tag{4.9}$$

Assume that we introduce a fluctuating electric field $\vec{E}$ to the system with fractional fluctuations $\epsilon(t) = (E(t) - \langle E(t) \rangle)/\langle E(t) \rangle)$ to the system. The Hamiltonian of the particle can now be modeled as [TKK+00]:

$$H(t) = \frac{\vec{p}^2}{2m} + \frac{m\omega_{sec}^2 \vec{x}^2}{2} - Qx\epsilon(t) \tag{4.10}$$

By separating the Hamiltonian into a stationary component, H_0, and a time-

dependent perturbation $H(t) = Qx\epsilon(t)$, time-dependent perturbation theory can be used to calculate the transition rate from the ground state to the first motional state $\Gamma_{0\to1}$. Adopting a simple one-dimensional model [TST97]:

$$\Gamma_{0\to1} = \frac{1}{\hbar^2}\left|\int_{-\infty}^{\infty} d\tau H(\tau)_{01} e^{i\omega\tau}\right|^2 \tag{4.11}$$

$$\Gamma_{0\to1} = \frac{1}{\hbar^2}\int_{-\infty}^{\infty} d\tau e^{i\omega_{sec}\tau}\langle\epsilon(t)\epsilon(t+\tau)\rangle\left|\langle 0|\, Qx\,|1\rangle\right|^2 \tag{4.12}$$

such that $\langle\epsilon(t)\epsilon(t+\tau)\rangle$ is the correlation function for fractional fluctuations in the field:

$$\langle\epsilon(t)\epsilon(t+\tau)\rangle = \int_0^{\infty} dt\epsilon(t)\epsilon(t+\tau) \tag{4.13}$$

Evaluating the matrix element $H(t)_{01}$, the transition amplitude is found to be:

$$\Gamma_{0\to1} = \frac{Q^2}{4m\hbar\omega_{sec}} S_E(\omega_{sec}) \tag{4.14}$$

where $S_E(\omega_{sec})$ is the Fourier transform of the fractional fluctuation correlation function and the spectral density of electric-field fluctuations. For an ion trapped by both static and oscillating electric fields, the change in thermal occupation number is found to be [WMI+98]:

$$\langle\dot{n}\rangle = \frac{Q^2}{4m\hbar\omega_{sec}}\left(S_E(\omega_{sec}) + \frac{\omega_{sec}^2}{2\Omega^2} S_E(\Omega \pm \omega_{sec})\right) \tag{4.15}$$

However, due to the radio frequency oscillations being larger and faster than the secular oscillations (by several orders of magnitude), the second term can be approximated as zero and ignored.

For the average metal at room temperature, the resistivity is approximately 1×10^{-8} Ohm-meters; therefore each electrode in a planar Paul trap has a resistance of approximately 2 Ohms. Noting the fact that the electric field will fall as $1/r^2$ for a distance d above the trap's surface, the voltage noise can be transformed into the

Noise	$\langle \dot{n} \rangle$	$S_E(\omega)$ $(\frac{V^2}{cm^2 Hz})$
Shot noise	$\frac{2Q^3\langle I \rangle R^2}{4m\hbar\omega_{sec}d^2}$	2.84×10^{-13}
Johnson noise	$\frac{k_b T R(\omega) Q^2}{m\hbar\omega_{sec}d^2}$	1.96×10^{-18}
Anomalous noise	$\frac{Q^2}{4m\hbar\omega_{sec}} S_E(\omega_{sec})$	$\frac{4m\hbar\omega_{sec}\langle \dot{n} \rangle}{Q^2}$

Table 4.1: The motional heating rate $\langle \dot{n} \rangle$ and electric field power spectrum $S_E(\omega)$ for the three sources of noise present in solids. No general analytical form is known for the power spectrum of anomalous noise, so no theoretical calculation can be performed.

electric field noise. Using $\omega_{sec} \approx 0.8$ MHz, m $= 1.455 \times 10^{-22}$ grams, d $= 150\mu m$, and $V_1 \approx 200$ Volts, the relative sizes of electric field noise can be computed as in Table 4.1

The analytical form of the power spectrum of anomalous noise is the general form for any noise – given the change of thermal occupation number in the trapped ion, the power spectrum can be computed. This is important because it allows the power spectrum to be measured to incredibly high precision – in single thermal quanta per second (on the order of 10^{-18} V^2 cm^{-2} Hz^{-1}). This makes trapped ions an unprecedentedly precise tool for measuring noise in solids.

4.2 Theory of Light-Induced Charging

As presented in Chapter 3, a variety of lasers spanning the entire energy spectrum from near-ultraviolet to the infrared is necessary for precise control of the trapped ion's state. Due to the small trapping distance between the ion and the electrodes, interaction of this light with the electrode material becomes very important. For the relatively low-energy wavelengths and electrode materials used in this experiment, the dominant surface-light interaction is predicted to be the photoelectric effect. The passivating oxide layers on the surface of aluminum and copper electrodes complicate the surface physics, trapping charges that are produced by photoemission and altering the trapping potential.

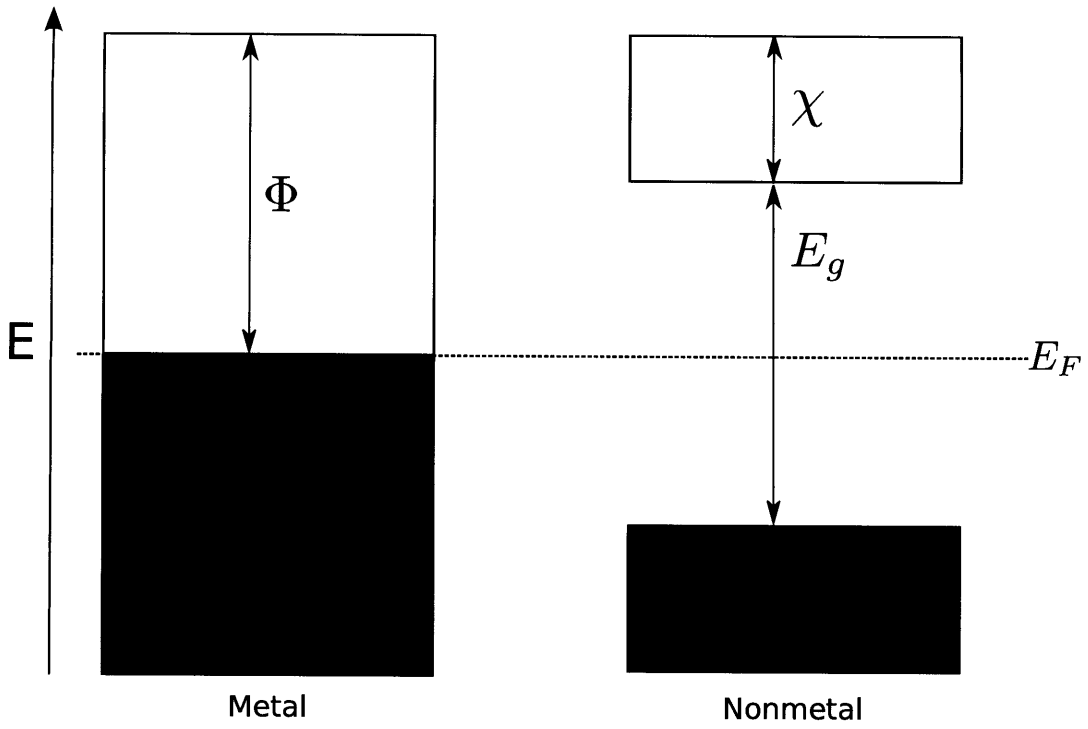

Figure 4-3: Examples of band structure for a single wave vector. On the left, the energy bands touch, making the material a metal. On the right there exists an energy gap, making the material an insulator or semiconductor based on the size of the gap. The dotted line represents the Fermi energy, E_F, and the filled in bands represent occupied energy states.

4.2.1 Band Structure of Metal-Oxide Systems

The complex band structure of solids gives rise to various types of materials depending on the size of the energy gap. When there is no energy gap (or a negative one such that the bands overlap), the material is a conductor. When there is a positive energy gap, the material is classified as a semiconductor (if the energy gap is on the order of a few eV) or an insulator (for large energy gaps). A simplified example of the band structure of a conductor and insulator for a single wavevector is shown in Figure 4-3.

There are two relevant characteristics given by the band structure of a metal: the Fermi energy E_F, and the work function Φ. The Fermi energy of any material represents the kinetic energy of the most energetic electron. A band diagram shows the allowed wave vectors; for nonmetals the Fermi energy lies in the forbidden region,

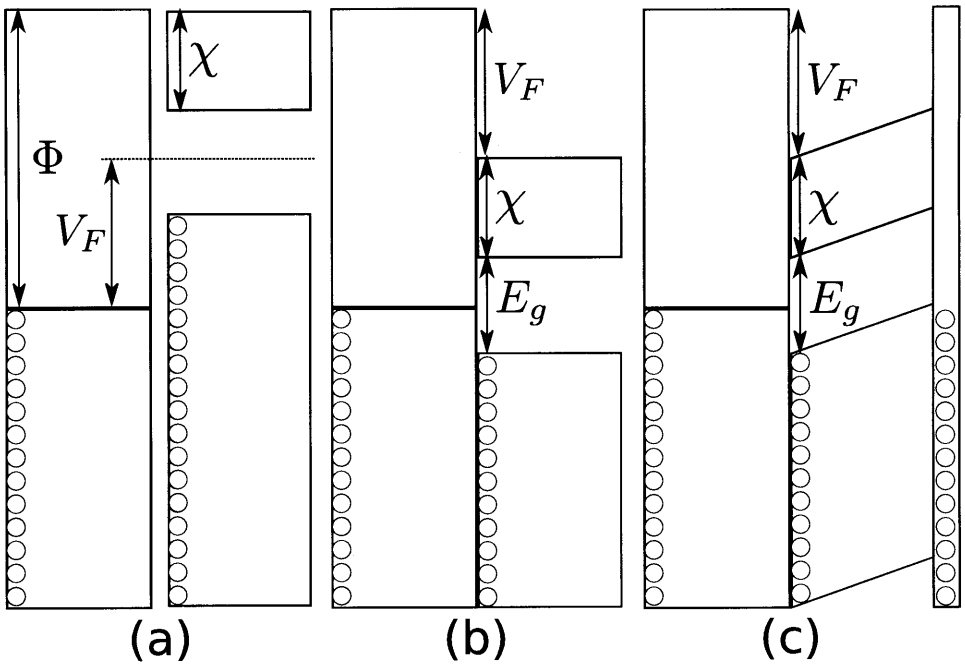

Figure 4-4: (a) The band structure of a metal and its corresponding oxide before contact is made. Circles represent electrons in the valence band. (b) The two materials are brought into contact, aligning their Fermi levels through charge transfer. This creates a new positive charge on the oxide and a voltage V_F is generate between the metal and oxide. (c) The addition of surface states (through adsorbates) can further alter the energy structure, "bending" the bands. The surface states can be filled via electron tunnelling through the oxide layer, and create a net negative charge on the electrode surface, creating a barrier between the electrons and the vacuum. In this diagram, Φ is the work function of the metal, E_g is the energy gap, χ is the electron affinity, and V_F is the difference in Fermi energies.

and the most energetic electron is in the most energetic allowed state in the valence band. The work function is the energy difference between the vacuum energy (the energy of the vacuum outside of the solid) and the Fermi energy. If an electron is imparted energy equal to its work function, then it will become free of the solid. For a nonmetal, the Fermi energy lies in the band gap, so the work function is equal to $\Phi = E_g + \chi$, where χ is the electron affinity.

When two different materials come into contact, their band structures must form a continuum of energy states. This is achieved by aligning the Fermi levels (see Figure 4-4b), accomplished by moving charge the material with the higher Fermi energy to

the material with the lower Fermi energy until the two are aligned. Figure 4-4a shows the band structure of a metal (left) and its oxide (right), assuming the oxide has a smaller work function (larger Fermi energy) than the metal. When the two materials come into contact, the Fermi energies align (Figure 4-4b) by transferring electrons from the oxide to the metal. In the case of passivated oxides, the metal's density of states is sufficiently large that the charge transfer does not alter the Fermi levels; however, the oxide layer is thin enough (and has a small enough density of states) that the oxide's Fermi level can change dramatically from the same charge transfer. The transfer of electrons from oxide to bulk metal creates a positive charge on the oxide in the process of aligning Fermi levels. This alters the work function of the oxide-metal system drastically due to the addition of the potential V_F. The total work function becomes

$$\Phi_T = \Phi - V_F \tag{4.16}$$

due to the lowering of the vacuum energy in the oxide relative to the metal. The potential V_F can be calculated easily as the difference in Fermi energies ΔE_F. However, in practice, the work function of the overall system is between Φ_T and Φ. This can be accounted for by the addition of surface states, as shown in Figure 4-4c. These energy states can be created by adsorbates, which are then filled by electron tunnelling through the oxide[Sem69], or by trapped charges in the oxide. The filling of these surface states creates a net negative charge on the surface on the oxide, creating a barrier for electron emission V_S. The total work function of the metal-oxide system, including surface states, is then given by:

$$\varphi = \Phi - V_F + V_S \tag{4.17}$$

By equating vacuum energies at the top of the band diagram, V_F can be found to be equal to $\Phi - E_g/2) - \chi$, assuming a band gap centered around the Fermi level. Substituting this into Equation 4.17, the metal-oxide work function can be written

$$\varphi = E_g + \chi + V_S \tag{4.18}$$

If the number of adsorbates is small (creating a small V_S on the surface) and the Fermi energy of the oxide is larger than the Fermi energy of the metal (such that V_F is positive), then the overall work function of the metal-oxide system is decreased. If the oxide has a lower Fermi energy than that of the metal, then the work function is increased.

4.2.2 Charging and Charge Dissipation on Metal Surfaces

Oxides are famous in the semiconductor industry for their ability to trap and hold charges for extremely long time periods. Therefore, electrons that are photoemitted from the bulk material can easily become trapped in the oxide before escaping. Over a finite period of time the charge will accumulate and build up on the surface, giving rise to a negative static surface charge that can perturb the trapping potential.

Charge accumulation and dissipation in a surface electrode ion trap can be modeled as a RC circuit with the metal's oxide as the dielectric layer in the capacitor. The equation for charge on a capacitor is given by

$$\dot{Q} = \frac{Q}{RC} \tag{4.19}$$

where R and C are the resistance and capacitance of the conducting material. The charges on the surface are created by photoemission in the metal induced by one of the lasers; let the rate of charge creation be K, where K is some constant rate that is a function of the laser and material parameters. Equation 4.19 can be modified to give

$$\dot{Q} = K - \frac{Q}{RC} \tag{4.20}$$

The electrode begins with zero surface charge ($Q(t = 0) = 0$), so the equation can be solved to give the total surface charge as a function of time

$$Q(t) = K\tau(1 - e^{-\frac{t}{\tau}}) \tag{4.21}$$

with time constant $\tau = RC$. For a slab of material with thickness L, area dA, dielectric constant ϵ_r, and resistivity ρ, these are given by $R = \rho L/dA$ and $C = \epsilon_0\epsilon_r dA/L$ where ϵ_0 is the permittivity of free space. For these values, the time constant is given by $\tau = \epsilon_0\epsilon_r\rho$. Due to the highly material-dependent nature of ρ and ϵ_0, this should be a highly material-dependent property. For typical values in an aluminum oxide surface layer ($\rho = 10^{14}\Omega cm$ and $\epsilon_r = 10$), τ is found to be approximately 100 seconds.

For the experimental setup used in this thesis, the laser that induces photoemission lies along the axial direction. Any charge that is created will become trapped along this line, creating a potential field given by

$$V_{line}(x, y) = \frac{Q}{2\pi L\epsilon_0} \ln\left(\frac{L + \sqrt{x^2 + y^2 + L^2}}{\sqrt{x^2 + y^2}}\right) \tag{4.22}$$

where L is the length of the line of charge (the length of the ground electrode in this particular setup). Such a potential is shown in red in Figure 4-5. The total potential near the trap minimum is given by the sum of the pseudopotential and the sum of line potentials $V_{line}(x, y)$ created from all photoemitted charges

$$V_T(x, y, dx, dy, n) = \left(\frac{Q^2V_1^2}{4mr_0^4\Omega}\right)^2 (x^2+y^2)+\frac{Q}{2\pi L\epsilon_0} \ln\left(\frac{L + \sqrt{(x + dx)^2 + (y + dy)^2 + L^2}}{\sqrt{(x + dx)^2 + (y + dy)^2}}\right) \tag{4.23}$$

such that dx and dy are the displacements of the line of charge from the charge center and n is the total amount of charge in the line. The superposition of the two potentials will shift the trap center (as shown in Figure 4-5, and the ion will be displaced. The displacement will cause micromotion with amplitude

x

$$A_{mm} = \frac{q}{2}|r| \tag{4.24}$$

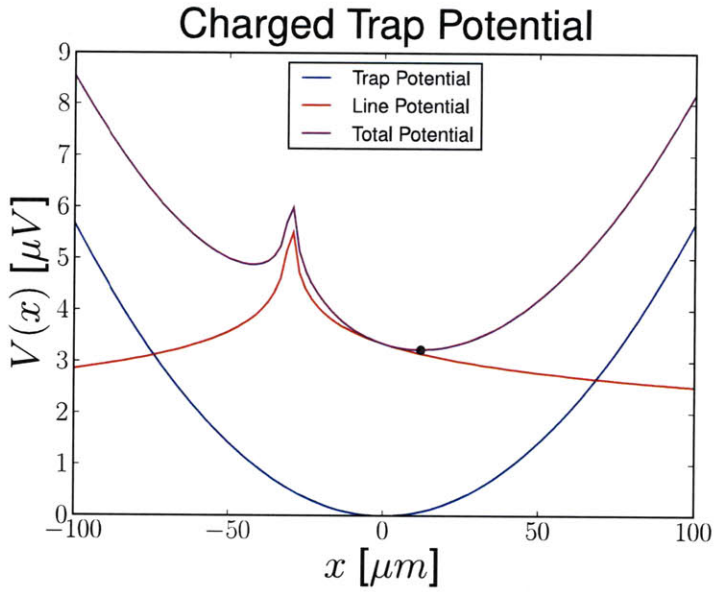

Figure 4-5: The trapping potential for a charged trap. The pseudopotential is shown in blue, and the potential due to the addition of a line of charge at $x = 30\mu$m from the trap center is shown in red. The superposition of the two is shown in purple, with the black dot showing the new center of the trapping potential.

where q is the Mathieu parameter and r is the displacement of the bottom of the potential well. Such micromotion can be detected as described in Section 3.4.2.

As charges continues to collect on the surface oxide, each charge contributes to the potential barrier V_S. As more charges accumulate, the barrier grows so large that photoemission can no longer continue. Therefore the process is self-limiting, and the charging of the surface electrodes is expect to converge towards a constant value.

4.3 Summary

This chapter introduced two important experiments that can be performed with trapped ions: measurements of heating rates and charging rates of the surface electrode trap. The relevant physics for each was discussed, followed with a methodology for how each measurement could be made using the theory from Chapters 2 and 3. In addition, theory was laid out for linking these measurements to much more fundamental physical phenomena – electric field noise and metallic work functions,

respectively. This concludes the theory portion of this thesis, and the rest of this document will detail the experimental apparatus used and the measurements that were taken.

Chapter 5

Fabrication

The surface-electrode architecture for ion traps introduced by Chiaverini *et al.* demonstrated many improvements upon the original linear quadrupole ion traps suggested by Paul [CBB+05]. The two-dimensional design allows for greater optical access and improves the scalability of the design. Perhaps the single greatest advantage of the planar design over the linear quadrupole one is the ability to apply the same microfabrication principles used in modern microelectronics to the manufacture of ion traps.

This chapter details the entire process of fabricating a planar ion trap from raw materials to the final packaging on the trap.

5.1 Wafer Preparation

The first step in microfabrication is the choice of a substrate. There are many possible choices for a substrate material, given that the only prerequisites for microfabrication are a relatively flat surface morphology and good adhesion to metal films. Possible substrates include fused silica, quartz, aluminum nitride, alumina, and diamond. Due to its high thermal conductivity and low dielectric constant (and therefore low RF loss), single crystal quartz was chosen as the substrate for the planar traps in this thesis. Beginning with a 3 inch single crystal quartz wafer, NR9-3000 photoresist is spun onto the wafer at 3000 rpm to protect the surface during the cutting process.

Using a diesaw, the wafer is cut into 1 cm by 1 cm squares. The photoresist is removed with acetone, and then the wafer proceeds to cleaning.

In the process of turning bulk quartz into wafers for distribution, the wafer is cut, polished, and packaged in a variety of steps. Inevitably, the wafer is exposed to a variety of unknown contaminants in this process. Organic contaminants include airborne bacteria, grease and oil from physical handling and cutting, abrasive particulates from cutting and polishing, and a variety of plastic particulates from the various packaging steps. In addition to organic contaminants, a variety of ionic impurities are also present. Improper cleaning and contaminated etchants can result in light ions (such as sodium and potassium) and heavy ions (such as gold, silver, copper, and nickel) contaminating the surface. The introduction of these ionic impurities can create electron traps and mid-gap states in the band structure of the bulk solid. In addition to the affecting the electronic properties, cleanliness is related to the adhesive properties of the film, and a dirty wafer can lead to a poor lithographic pattern. The chemical removal of these contaminants is the first step in the fabrication process.

The first step is a basic degreasing in sequential baths of acetone, isopropanol, and deionized water. The solvents remove any oils and greases remaining on the surface from handling. Acetone is used first because it is a much stronger solvent, and isopropanol is used second due to its lower volatility (resulting in fewer streaks of dissolved greases). The wafers are then rinsed in deionized water and blown dry with nitrogen gas.

The next step is to remove the large particulates on the surface. These include remaining abrasives used in polishing, and fractured quartz particulates left from cutting the wafers. Hydrofluoric acid cannot be used to remove these silica particulates because it will dissolve the quartz substrate; the uneven distribution of particulates on the surface would result in a highly uneven surface. The best solution is to use a simple mixture of soap and deionized water. The soap forms micelles around the particulates, which are easily removed with a rinse in deionized water.

The wafer is then cleaned using a solution of concentrated sulfuric acid (H_2SO_4) and 30% hydrogen peroxide (H_2O_2) in a 3:1 volumetric ratio. The wafer is submerged

in the solution at room temperature for 15-20 minutes before being removed, rinsed with deionized water, and blown dry with nitrogen gas. This solution is used primarily to remove organic residue and photoresist from the wafers. The sulfuric acid dehydrates organic substances by stripping them of their hydrogens and oxygens to create water molecules. The sulfuric acid converts hydrogen peroxide to hydronium, which acts as a strong oxidizing agent to create CO_2 gas, which bubbles out of the solution.

The final step in cleaning is immersion in a solution of ammonium hydroxide (NH_4OH), hydrogen peroxide (H_2O_2), and deionized water (H_2O) in a 1:1:5 volumetric ratio. The solution is heated to 80° C, and then the wafer is left in the solution for 15-20 minutes. The wafer is then removed, rinsed with deionized water, and blown dry with nitrogen gas. The hydrogen peroxide acts as an oxidizing agent, oxidizing any light metals or remaining organic contaminants. The ammonium hydroxide removes heavy metals from the substrate by reacting with them to form complex -amine groups, which then fall into solution from the substrate surface.

5.2 Lithography

Once a clean wafer is achieved, the next step is the print the desired pattern on the metal. The basic premise is to apply photoresist to a substrate, and then expose the photoresist through a mask to ultraviolet light. The ultraviolet radiation denatures the photoresist where there are gaps in the mask, leaving the remaining photoresist unaffected. The remaining photoresist is then immersed in a developing agent (as specified by the photoresist manufacturer), which dissolves the denatured photoresist but leaves the unexposed regions unaffected. Finally, the patterned resist is used to either additively or subtractively print metal on the substrate. The remaining resist can then be dissolved in acetone and removed from the completed wafer. In this thesis, two photolithographic processes are explored – a subtractive process involving the chemical etching of material from the wafer, and an additive process known as the lift-off technique.

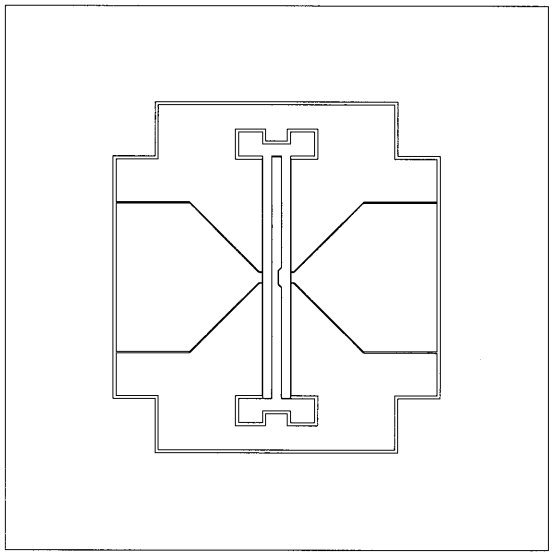

Figure 5-1: The pattern on the chrome optical mask used for photolithography.

The etching technique begins with the physical vapor deposition of the desired electrode material onto the clean substrate. Using electron beam evaporation, 400 nm of the desired material is evaporated onto the substrate. For copper and gold electrodes, a 10 nm layer of Ti is evaporated first as an adhesion layer. Following evaporation, the wafers are placed on a hotplate at 150° C for 5-10 minutes to drive out any moisture that may have accumulated in storage. This drying process ensures that the photoresist is applied evenly and that the pattern transfers well. Next, NR9-3000P photoresist is spun onto the electrode material at 3000 rpm for 60 seconds, and then baked for 60 seconds at 150° C to harden the resist. The resist is then exposed with a 3400 μW cm^{-2} source for 120 seconds through a mask with the desired pattern on it. The pattern used is shown in Figure 5-1. The wafer is then baked again at 90° for 120-180 seconds. The patterned wafer is then developed in RD-6 Developer for 17 seconds or until the pattern is completely visible, and then rinsed with deionized water and dried with nitrogen gas. The wafer is baked one final time for 120 seconds at 90° to complete the pattern transfer.

After the pattern has been successfully transferred, the next step is to acid etch the exposed metal away. For aluminum, a phosphoric acid-based etchant was used (H_3PO_4, HNO_3, CH_3COOH, and H_2O in a 16:1:1:2 ratio) to remove the exposed

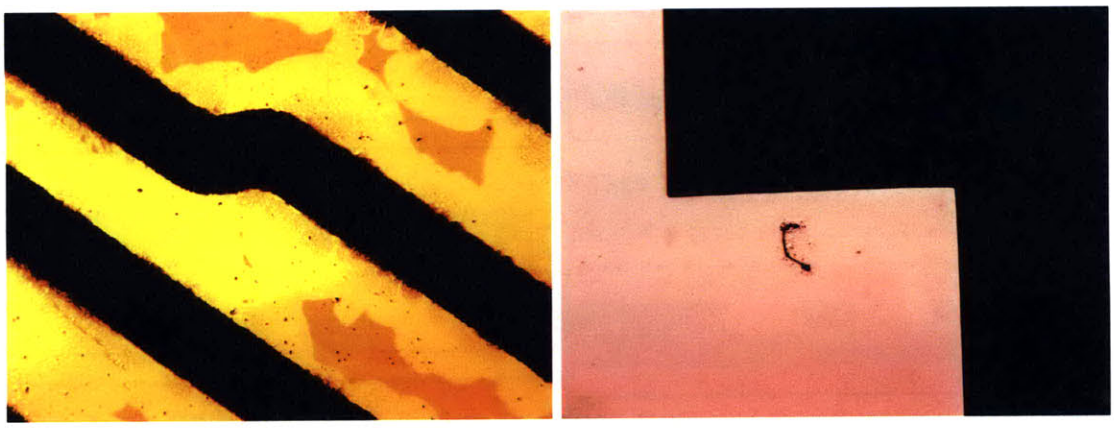

Figure 5-2: A comparison of the edge quality for etched traps (left) and a trap fabricated using the liftoff technique (right).

material. This etch also etches away the Al_2O_3 passivation layer, meaning that no other etchant is necessary. For copper, a solution of Aqua Regia was used (HCl, HNO_3, and H_2O in a 3:1:2 ratio). For all etchants, the wafer was left in the solution until all electrode material had dissolved into the etchant and the gaps were visibly defined.

In past traps the edge quality has been found to be extremely important to trap performance. During use, the electrodes may have a potential as high as 200 V applied across a 10 μm gap; the electric field easily exceeds the breakdown voltage, dielectric breakdown commences, and the trap is rendered useless. For the silver and gold traps used in past experiments, the solution was found to be thermal treatment of the traps. By annealing the traps, the bulk material would recrystallize and the electrode edges would become smooth again. However, aluminum and copper are not nearly as inert as gold and silver and form thick oxide layers quickly, making thermal treatment counterproductive. Lift-off patterning was used instead in order to create smoother edges between the electrodes.

The lift-off technique is an additive process where material is selectively added to the wafer in the desired areas. The same pattern transfer is utilized as before with the exception of no final bake and that in the lift-off technique the pattern is transferred directly to the clean quartz wafer. The electrode material is then directly evaporated onto patterned photoresist, filling in the gaps in the pattern with metal.

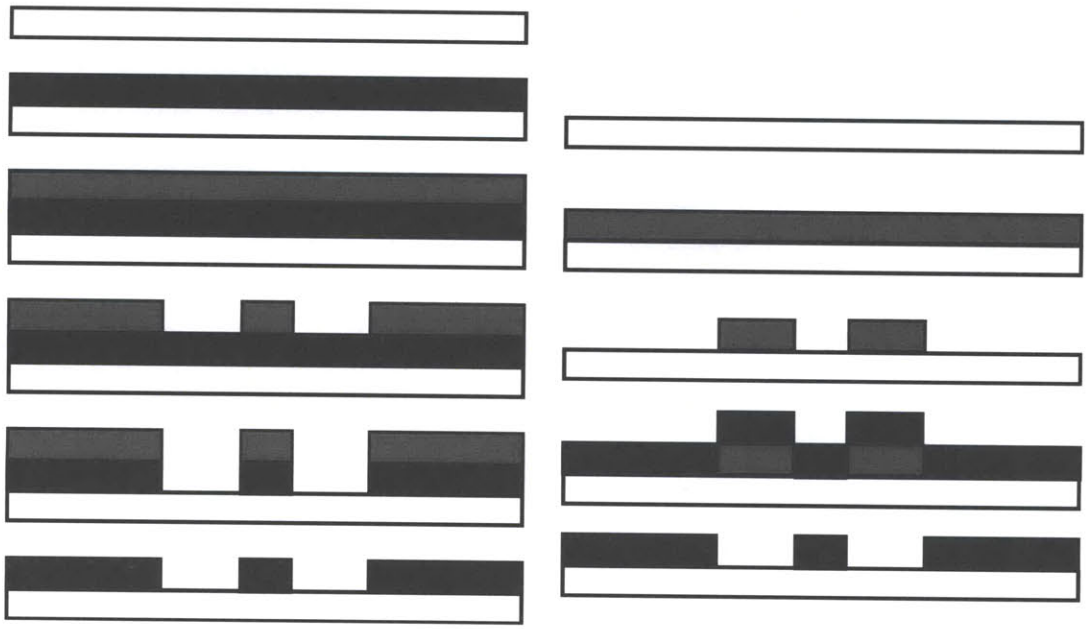

Figure 5-3: A comparison of the photolithographic processes for the etching process (left) and the liftoff process (right). In both images, the quartz substrate is white, the metal is black, and the photoresist is grey. The narrowest part of the middle electrode on the left is 150 μm.

A different mask is needed due to the additive nature of this process; a negative of the previous mask was made for this purpose. The wafer is then soaked in acetone for 10-20 minutes; this dissolves the photoresist, and "lifts off" the metal evaporated onto the photoresist. Any metal deposited directly onto the wafer is left unaltered.

It was found that the lift-off method gave a much higher edge quality, and avoided the issues of overetching the material. In addition, the surface of the metal was found to be much cleaner due to less exposure to organic contaminants in the photoresist. Both the lift-off process and the etching process are summarized in Figure 5-3.

The gold trap was fabricated using a separate method that involved using a quartz wafer with titanium and silver evaporated onto it used as the substrate for gold. The gold layer itself was patterned using the above lift-off method, and then electroplated. The adhesion layers were removed with appropriate etchants.

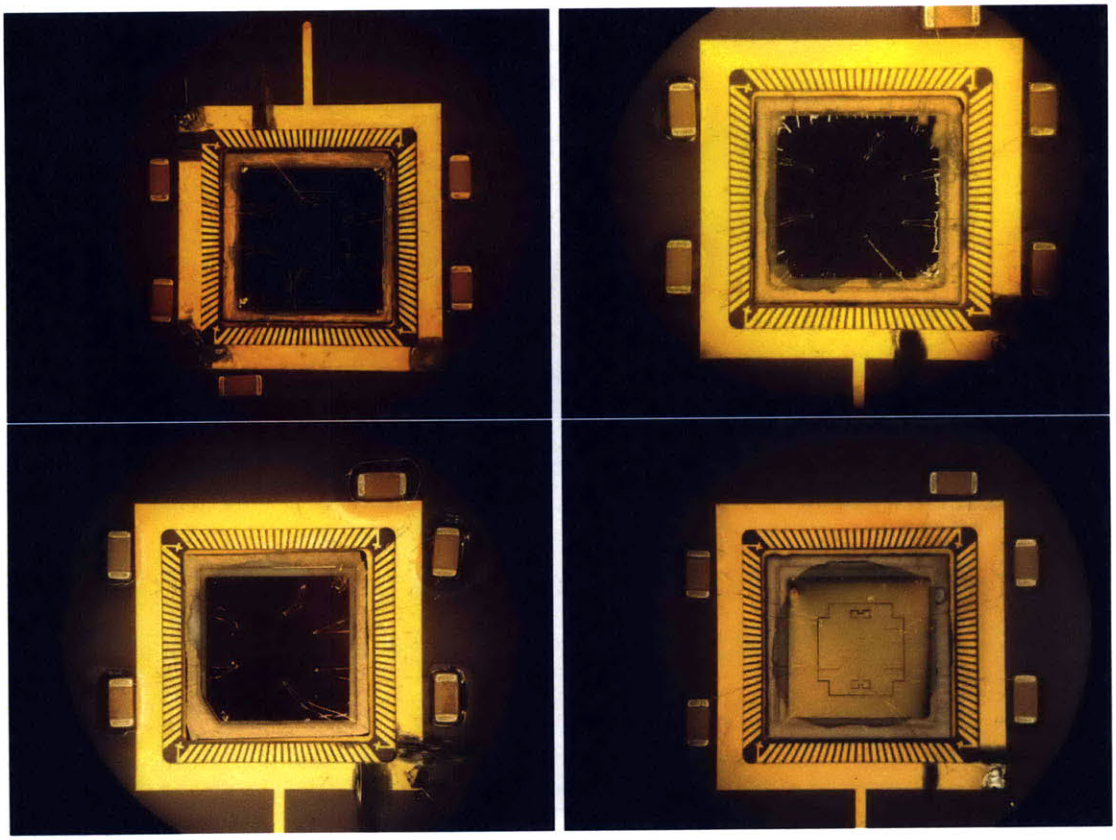

Figure 5-4: Examples of completely patterned traps mounted in a Ceramic Pin Grid Array. From top left to bottom right, the traps are made out of aluminum, aluminum oxide, copper, and gold. Each microfabricated trap is 1 cm $\times$ 1 cm. The packaging process is discussed in Section 5.3

5.3 Packaging

The final stage of the fabrication process is that of turning the patterned heterostructure into a full-fledged microelectronic device. The wafer is placed in a ceramic pin grid array (CPGA) as the substrate for packaging. The CPGA and a niobium spacer are soaked and agitated by ultrasonication in baths of soap and deionized water (to remove dust and particulates) and acetone (to dissolve organic contaminants). The niobium spacer is then epoxied with Torrseal (Variac, Inc) to the center of the CPGA to elevate the surface of the trap such that it is flush with the surface of the CPGA. The quartz wafer is bonded to the niobium spacer with epoxy, and the entire CPGA is then heated at 70° C for an hour to cure the epoxy.

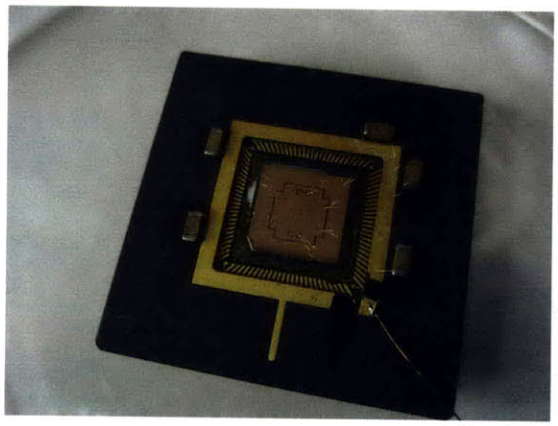

Figure 5-5: A completely packaged copper trap mounted on CPGA. The trap size is 1 cm $\times$ 1 cm

1 nF capacitors (AVX GH0358102KN6N) are then secured to the ceramic surface of the CPGA using cyanoacrylate (SuperGlue). These capacitors serve as low-pass filters, reducing RF pickup and noise on the electrodes. Each of the capacitors is wirebonded using gold (for gold and copper traps) or aluminum (for aluminum traps) wires to the CPGA pads. Then each electrode on the trap is wirebonded to two pads on the CPGA (to allow for redundancy in case one of the wirebonds fails).

5.4 Summary

This chapter summarized the entire fabrication process starting from a single crystal quartz wafer to a finished product. After an extensive cleaning regimen, the traps are patterned and electrode material is added via physical vapor deposition techniques to the quartz wafer. Tests demonstrated that the lift-off technique for pattern transfer resulted in a much higher resolution pattern on the finished wafer, so the lift-off method was used for the traps fabricated as part of this thesis. The fully patterned wafer is then packaged in a CPGA in order to make the device compatible with preexisting electronics. The result is a CMOS-compatible microfabricated ion trap.

Chapter 6

Electric Field Noise and Light-Induced Charging: Measurements

The focus of this work is to explore material alternatives to gold ion traps, due to gold's incompatibility with CMOS-based technology. However, in order for any material to supplant gold as a frontrunner for an electrode material, it must exhibit a similar performance to gold. So far this work has explored the dynamics and fabrication of ion traps, the energy structure of trapped strontium ions, and the characterization of noise and charging effects on metallic surfaces. The culmination of this work is to use the measurement methods detailed in this document to compare the electric field noise and surface electrode charging in various materials. Previous work has demonstrated the gold surface electrode traps exhibit electric field noise on the order of 10^{-18} V^2 cm^{-2} Hz^{-1}, which should approach the Johnson noise as demonstrated in Section 4.1.3[LGA+08]; this thesis seeks to determine whether aluminum and copper surface electrodes can exhibit similar performance. If such performance can be achieved, then aluminum and copper may be even more ideal candidates for surface electrode ion traps due to their compatibility to CMOS technology.

Eleven traps were tested as part of this thesis. In total, nine traps were made with aluminum as the electrode material; out of these nine traps three had aluminum

oxide deposited on the electrodes to measure the effects of the oxide layer on the measurement. In addition to the aluminum traps, two final traps were fabricated that used copper and gold as their electrodes, respectively. This chapter presents the measurements of electric field noise and electrode charging rates in these traps at cryogenic temperatures. For each experiment, the setup is described in detail and the results are presented, followed by an interpretation of the measurements taken.

6.1 Heating Rates in Trapped Ions

6.1.1 Heating Rate Measurements

At the cryogenic temperatures used in this experiment, the electric field noise spectral power due to Johnson noise is on the order of 10^{-18} V^2 cm^{-2} Hz^{-1} [Lab08]. Shot noise should not exist because the surface electrodes do not draw current. Therefore, any noise measured larger than the Johnson noise should be of anomalous nature; if the anomalous noise is completely suppressed then only the Johnson noise should remain.

The measured noise in the electrodes should be independent of material to within an order of magnitude, as described in Section 4.1.2. However, without a clear idea of what processes are the source of anomalous noise, it is unclear how the existence of a surface oxide will affect heating rates. Unoxidized aluminum and copper should behave similar to gold to first order, while the exact behavior of oxidized electrodes in unclear.

The first measurement taken for each trap was a measurement of the heating rate of the motional mode. Each trap was mounted in the cryostat, which was then evacuated to 10^{-5} torr and cooled to liquid helium temperature with cryogens. After cooling, the cryostat pressure is expected to be better than 10^{-10} torr. The cryostat is described in much more detail in Chapter A. Typical trap operating parameters were approximately 190 Volts at 36 MHz with compensation voltages $V_2 = V_3 = -V_4$ = 10 V and V_5 = -13 V. Single $^{88}Sr^+$ ions were loaded via evaporation of neutral

strontium and photoionization (as described in Section A.2 and Doppler cooled to < 1 mK. The ion was then sideband cooled on the $S_{1/2} \rightarrow 4D_{5/2}$ transition to the motional ground state within about 150 cycles.

Once the ground state was reached, heating rates were determined by measuring the transition amplitudes for the red and blue sidebands after a delay time. A typical delay was on the order of 1-5 milliseconds, with delays reaching as high as 25 milliseconds for some of the longer measurements. The heating rates (measured in quanta per second) were then converted into electric field noise spectral density $S_E(\omega)$ as shown in Table 4.1 to remove dependencies on the ion mass and secular frequency and allow for better comparison to values from the literature. The data is shown in Table 6.1.2.

6.1.2 Results and Discussion

The first two generations of aluminum traps exhibited poor ion lifetimes (on the order of seconds), making it exceedingly difficult to measure the heating rates. These traps were fabricated using a trap geometry that trapped the ion 75 μm above the trap surface and the chemical etching technique discussed in Chapter 5. The extensive use of chemical etchants could easily contaminate the surface and contribute to short ion lifetimes. The ineffectiveness of the first two trap generations led to the use of a larger trap geometry (with a trap height of 100 μm). Electric field noise has been found to follow an inverse power-law relationship with ion-electrode distance (d^{-4}), so an increase in trap size should result in a more stable trap [DOS+06].

Section 4.1.2 suggested that anomalous noise should exhibit little to no materials dependence; the data supports this claim. Earlier heating rate experiments with this setup used gold and silver traps and found the heating rates to be on the order of 10^{-18} V^2 cm^{-2} Hz^{-1} [Lab08]. The lowest measurements from Al-IIIb and Al-IIIc are on par with the smallest observed heating rates in the previous work, with Cu-I performing on par with the hotter traps in the same work. Despite thin passivation layers of oxide on the surface, both aluminum and copper electrodes performed as well as gold and silver in cryogenic surface electrode traps.

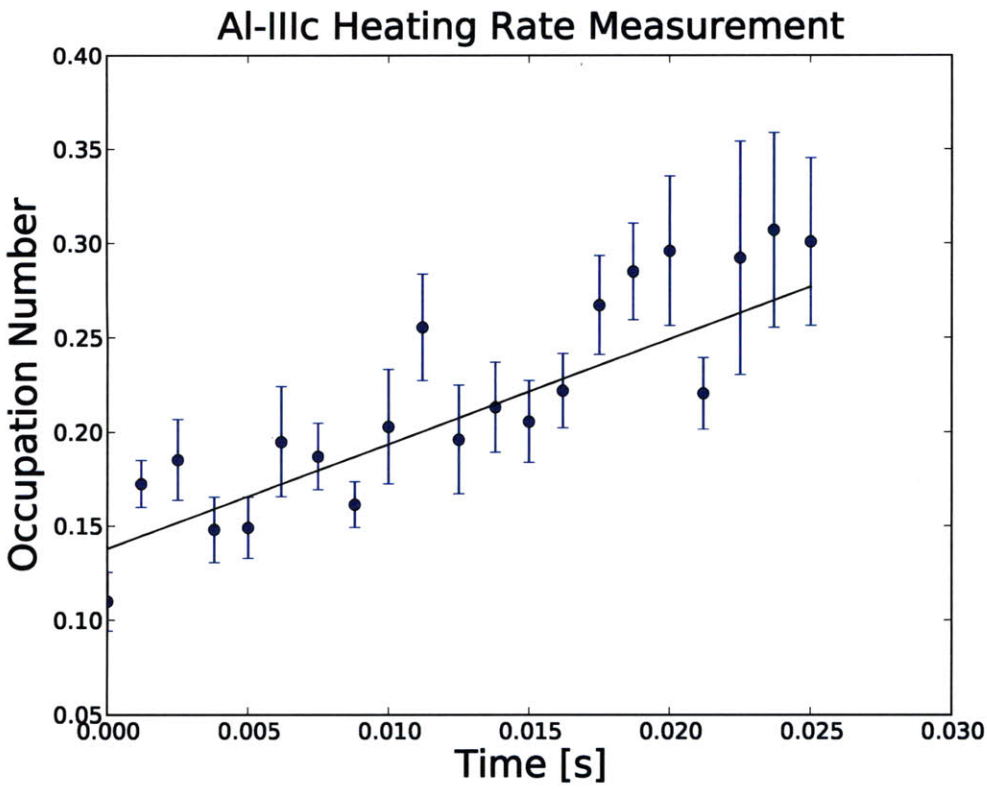

Figure 6-1: Sample plot of occupation number versus delay time. The heating rate can be extracted as the slope of the fit line (black), which is then converted in an electric field noise $S_E(\omega)$. Error bars signify one standard deviation from the mean value.

The data indicates that the presence of an oxide layer is correlated to the electric field noise. With as little as 5 nm of deposited oxide, the electric field noise increased by an order of magnitude. This suggests an exponential dependence upon oxide thickness; a factor of two in oxide thickness corresponds to over a factor of 10 in electric field noise. The noise in Al_2O_3-10 was abnormally high compared to the Al_2O_3-20; however, the measurements only provide an upper bound on the minimum heating rate, so it is still possible that 10 nm of deposited oxide has a lower possible heating rate given appropriate trapping parameters. In addition, variables introduced during the processing (cleanliness of the substrate, purity of the film) and handling may be responsible for high heating rates.

The data appears to approach a limit as the oxide layer increases; therefore the

Material	$S_E(\omega)$ $(10^{-18}\ \frac{V^2}{cm^2 Hz})$	ω_{sec}	Trap Size	Thickness	Oxide
Al-I	-	0.896 MHz	75 μm	1.5 μm	Native
Al-IIa	-	-	75 μm	1.2 μm	Native
Al-IIb	-	-	75 μm	1.2 μm	Native
Al-IIIa	9.32 $\pm$ 1.4	0.750 MHz	100 μm	400 nm	Native
Al-IIIb	1.33 $\pm$ 0.16	0.796 MHz	100 μm	400 nm	Native
Al-IIIc	1.31 $\pm$ 0.16	0.816 MHz	100 μm	400 nm	Native
Al_2O_3-5	67.5 $\pm$ 5.5	0.800 MHz	100 μm	400 nm	5nm
Al_2O_3-10	197 $\pm$ 22	0.788 MHz	100 μm	400 nm	10 nm
Al_2O_3-20	176 $\pm$ 12	0.836 MHz	100 μm	400 nm	20 nm
Cu-I	16.5 $\pm$ 1.7	1.006 MHz	100 μm	400 nm	Native

Table 6.1: The lowest electric field noise $S_E(\omega)$ observed for each trap tested. The roman numeral after the material name indicates the generation number of the trap; all traps with the same roman numeral were fabricated simultaneously using the same procedure. The letter following the numeral is a unique identifier for the trap within the generation. A representative plot of the raw heating rate data is shown in Figure 6-1.

data was fit to a $d_0(1 - e^{-\frac{d}{\delta}})$ type function, such that d_0 is the saturation noise and δ is the characteristic lengthscale of the noise. Fitting to this type of curve (shown in Figure 6-2, the saturation noise is found to be $2.4 \pm 0.4 \times 10^{-16}$ V^2 cm^{-2} Hz^{-1}. The characteristic lengthscale is $\delta = 13 \pm 3$ nm; therefore the thickness dependence should be strongest for oxide layers thinner than 13 nm.

6.2 Light-Induced Charging

6.2.1 Electrode Charging Measurements

The second experiment measured the light-induced charging of the surface electrodes of each ion trap. After the trapped ion was cooled to its motional ground state as described in Section 6.1.1, micromotion was observed using the cross-correlation method described in Section 3.4.2. Typical observed micromotion was sensitive to 0.01 V change in compensation voltages. Three different lasers were lowered along the axial direction on the trap until the beam grazed the surface. The laser was held there for up to 20 minutes while the micromotion was measured as a function of time. From the micromotion amplitude, the time constant and charging rate were extracted

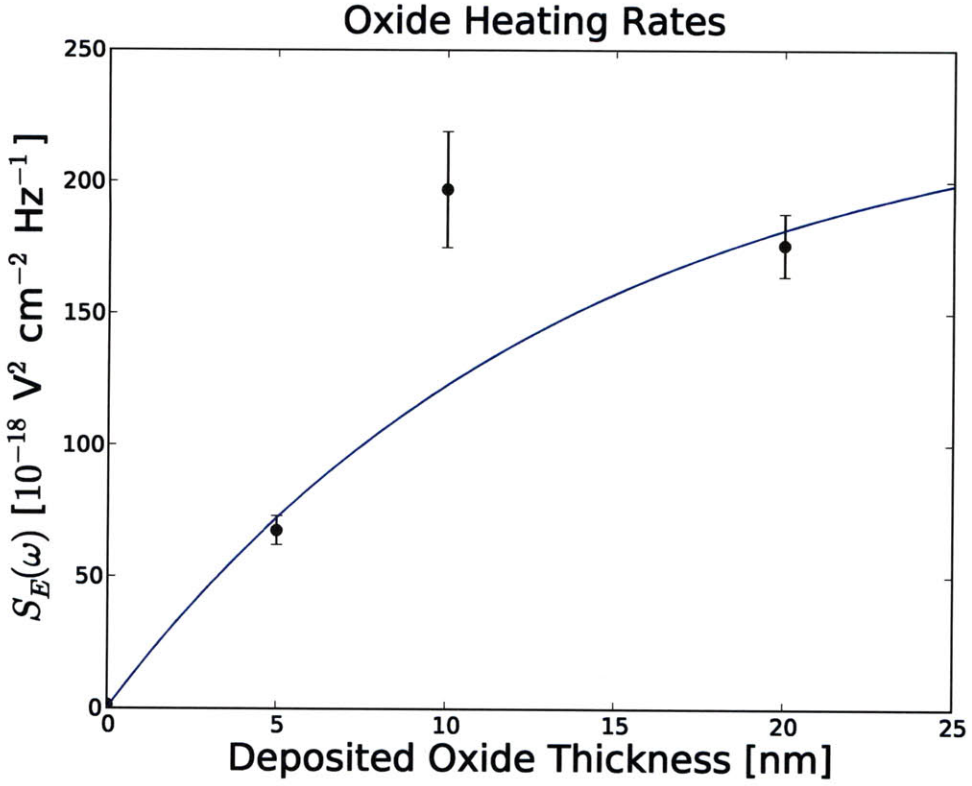

Figure 6-2: The heating rate of aluminum traps with aluminum oxide deposited on the surface of the electrodes. The heating rate appears to follow a $d_0(1 - e^{-\frac{d}{\delta}})$ type relationship. For this data set, $d_0 = 236 \pm 39 \times 10^{-18}$ V^2 cm^{-2} Hz^{-1} and $\delta = 13 \pm 3$ nm. Note that traps with zero deposited oxide still possess a surface oxide of $\approx$ 2-3 nm. The half-width of the error bars signify one standard deviation from the mean.

using the theory presented in Section 4.2. The key parameters of the three lasers used in these measurements are listed in Table 6.2.

The work functions of the materials used as electrodes are 4.26 eV (aluminum), 5.10 eV (copper), and 5.47 eV (gold); therefore, photoemission would not be expected in any of these materials. However, as discussed in Section 4.2.1, the presence of a metal oxide can perturb the work function in a material. Therefore it is possible that aluminum and copper will emit photoelectrons if an oxide is present. The electron affinity of aluminum is 1.95 eV and the band gap is 6.95 eV [Miy01]; using these values in Equation 4.18 the metal-oxide work function is found to be $\phi_{Al2O3} = 5.5$ eV. This is larger than the work function of aluminum; therefore electrons will charge the

Wavelength	Beam Waist	Power	Photon Flux ($\frac{photons}{cm^2 sec}$)	Energy
405 nm	170 μW	100 μm	1.9×10^{35}	3.06 eV
460 nm	100 μW	100 μm	1.3×10^{35}	2.72 eV
674 nm	300 μW	34 μm	4.7×10^{36}	2.08 eV

Table 6.2: Relevant laser parameters for the optics used in the charging experiment. The above assumes a geometry with a 1° angle of incidence onto the electrode surface and an electrode length of 5 mm.

oxide and the oxide will serve as a barrier for photoemission.

Copper oxides, however, have a Fermi energy higher than that of coppper, therefore the oxides lower the work function. For the first oxide of copper, copper (I) oxide, the electron affinity is 1.10 eV and the energy gap is 2.13 eV. Performing the same computation as for aluminum, the new work function of the metal-oxide system should be $\varphi_{Cu2O} = 2.16$ eV. The second oxidation state, copper (II) oxide, possesses an electron affinity of 2.12 eV and an energy gap of 1.2 eV, resulting in a work function of $\varphi_{CuO} = 2.72$ eV. In reality copper oxidizes into a mixture of the two, so the observed work function should lie between these two extrema. From the computed metal-oxide work functions, it is predicted that the 405 nm and 460 nm laser will cause electrons to be photoemitted and trapped in the oxide; however, the 674 nm laser should not.

The measurement was taken by lowering a laser in the axial direction until the laser grazed the surface of the trap (as shown in the CCD camera). The micromotion was then measured using the cross-correlation technique described in Section 3.4.2 to provide a measure of the charging on the electrode surface over a period of several minutes (typically between 10 and 20 minutes). Ion traps Al-IIIc, Cu-I, and Au-I were used for the charging experiment. In addition, charging was measured in Al_2O_3-10 to measure the influence of oxide thickness.

6.2.2 Results and Discussion

The results are shown in Table 6.3. Aluminum electrodes exhibited charging when irradiated with the 405 nm laser, but did not exhibit charging due to any of the

Trap	405 nm	460 nm	674 nm
Al-IIIc	$\tau = 600$ s	-	-
Al-10	$\tau = 500$ s	-	-
Au-I	-	-	-
Cu-I	-	-	$\tau = 140$ s

Table 6.3: Results of light-induced charging of surface electrodes for four different traps. Both of the aluminum traps charged when irradiated with 405 nm light, while the copper trap only charged when exposed to 674 nm light. The gold electrodes did not charge during any of the experiments. The characteristic timescale for saturation of electrode charge is shown for all traps that exhibited any charging behavior to within approximately 20%.

higher wavelength lasers. Figure 6-3 shows the raw data collected for the aluminum trap. Copper did not exhibit any charging for the lower wavelength lasers, and instead charged when the 674 nm laser was incident on the surface. Gold exhibited no charging for any wavelength of laser, for up to 10 minutes of exposure time.

The existence of charging on the surface electrodes of Al-IIIc is highly unexpected. However, Section 4.2.1 predicted that the presence of surface states (via adsorbates or metal-induced gap states) could potentially allow for photoemission. Using Equation 4.18, the surface charge must be between 3.5 eV and 3.85 eV to produce the observed photoemission in aluminum metal. Applying the same equation to copper, the surface charge on the copper electrodes must be between 0.32 eV and 0.88 eV. The surface charge would need to be positive in order to cause the indicated voltage drop, suggesting that adsorbed strontium ions or metallic contaminants would be the source of the charge.

Assuming a material-independent adsorbate, the measurements indicate that the total voltage drop due to adsorbates on the surface would need to be at least 3.5 eV to induce photoemission in aluminum. This is more than sufficient for copper, and would decrease the effective work function such that very little energy would be necessary to remove electrons from the bulk metal. This is in agreement with the extremely fast charging rate observed in copper ($\tau_{Cu} = 140$ s) relative to aluminum ($\tau_{Al} = 600$ s). The lack of photoemission due to the higher energy photons could potentially be described by some absorption-driven phenomena, as copper is well-known for its

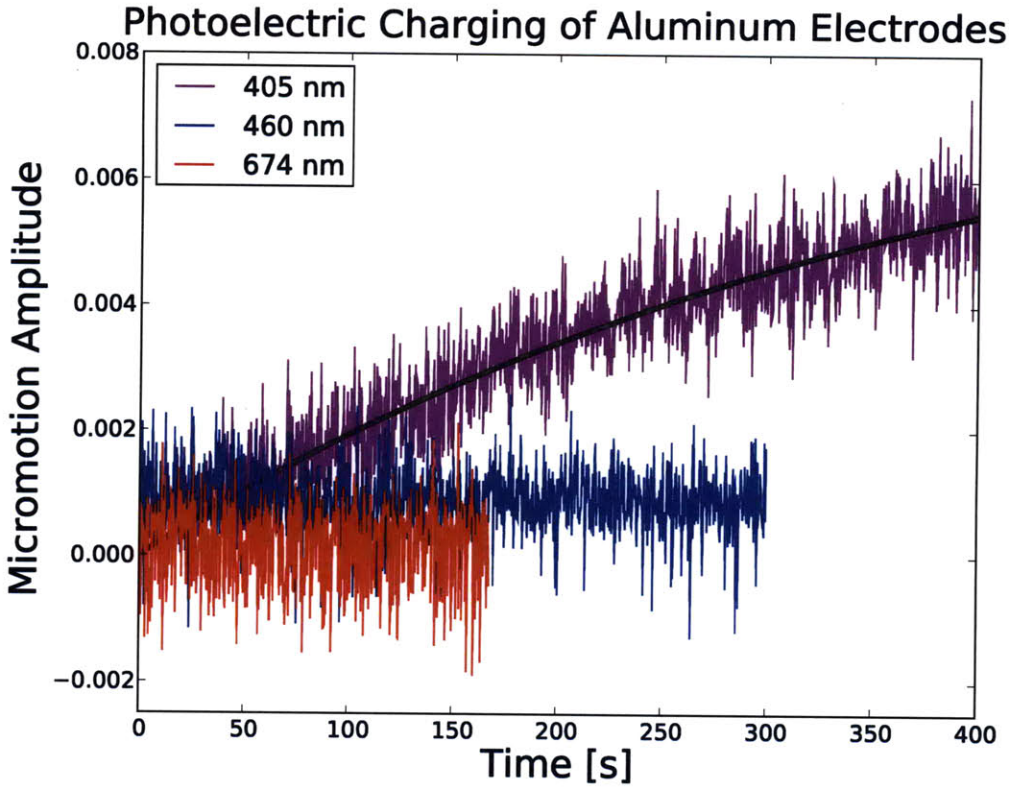

Figure 6-3: Sample plot of micromotion versus exposure time for an aluminum surface electrode exposed to a laser. The total charge on the electrode can be deduced from this change in micromotion, and the charging rate τ can be determined. Only the 405 nm (purple) laser caused an increase in micromotion amplitude; 460 nm (blue) and 674 nm (red) lasers did not exhibit any change in micromotion. The time constant was determined to be $\tau \approx 600$ seconds, of the same order of magnitude as predicted.

absorption of blue and ultra-violet radiation.

Solving for the charge creation rate K from the experimentally determined time constants, it is found to be approximately 10^4 charges per second for the tested traps. According to the model presented in Section 4.2, all charges are due to photoemission in the bulk material; therefore the charge creation rate should be related to the incident photon flux. The values in Table 6.2 indicate a photon flux on the order of 10^{32} photons per second; a discrepancy of over 28 orders of magnitude. However, the density of atoms on a given surface is only on the order of 10^{12} for all materials tested, indicating that the discrepancy is closer to 8 orders of magnitude. The large discrepancy between the incident photons, absorption sites, and charge creation rate

implies that there is some type of efficiency in conversion from photons to charges that must be accounted for.

A possible mechanism for the discrepancy between charge creation and the theoretical yield for photoemitted electrons is tunneling through the oxide layer. If the oxide layer was treated like a potential barrier, then the photon must tunnel through the barrier to reach the surface. In order to see 10^{-8} fewer electrons than photons, the oxide barrier would need to be 6 nm thick. A typical passivation layer is approximately 2-3 nm thick, so tunneling would initially seem plausible. However, the transmission coefficient should decrease exponentially with barrier size; this behavior is not consistent with the observations of charging rate in Al_2O_3-10, which has nearly the same charging rate and a significantly thicker oxide layer. This model has inspired similar models which use the band-bending length (on the order of 1-3 nm) as the barrier heights; such models show much more promise for accurately describing the observed data.

When the incident laser beam was blocked, both aluminum and aluminum oxide traps exhibited constant micromotion at the increased rate for several minutes. This suggests that the discharge rate is significantly longer than the charging rate, implying that the discharge rate is not the limiting factor to the charge rate. Thus it is likely that a surplus of trapped negative charge in the oxide layer is responsible for the saturation of charging rate in aluminum traps, and that the charging mechanism is due to trapped charges in the oxide.

6.3 Summary

This chapter presented the results of heating rate measurements and photoelectric charging in aluminum, copper, and gold surface electrode traps. The former set of measurements demonstrated that heating rates approaching the Johnson noise limit are possible with aluminum traps, and suggests that it may be possible to achieve similar results with other materials. Additionally, it was demonstrated that the growth of oxide layers on the electrodes has a significant effect on heating rates

in trapped ions.

The latter experiment demonstrated that aluminum and copper ion traps exhibit charging phenomena for specific wavelengths, but gold electrodes are immune to the same phenomena. Inconsistencies were seen in both the photoemission spectrum of copper and aluminum and in the charging rates. A negative surface charge on the order of 3.3 eV would be necessary to explain the data with the current model, suggesting an error with our model. The charging rate was determined to be several order of magnitudes smaller than the postulated mechanism predicted, suggesting that much more complex phenomena other than photoemission may be involved. Further work is needed to quantify and fully understand the mechanism behind light-induced charging.

Chapter 7

Conclusions

7.1 Summary

This thesis documents the fabrication of several series of surface electrode traps for use in ultra high vacuum environments at cryogenic temperatures. Initial experiments demonstrated that surface electrode traps made from aluminum and copper can have comparable performance to gold traps while maintaining the advantage of being CMOS-compatible metals. This helps support the case for using CMOS fabrication techniques to fabricate arrays of surface electrode ion traps for large-scale quantum computing.

Using microfabrication techniques, a procedure for the rapid production of surface electrode ion traps was formulated, resulting in the complete fabrication of an ion trap in 12-15 man-hours. A thorough yet efficient cleaning regimen was determined to provide a clean surface for electrode deposition, and several lithographic processes were explored. The best method was found to be the lift-off technique, which created smooth enough edge finishes that electrostatic breakdown was not a problem at operating voltages and further processing was not necessary. At least one generation of each trap was fabricated that successfully trapped single $^{88}Sr^{+}$ ions at cryogenic temperatures, demonstrating that it is possible to make effective ion traps out of metals with passivating oxides.

Each of these ion traps was then characterized by making a series of heating rate

and charging rate measurements. By observing the dynamics of a trapped ion over time, fluctuations in the electric field could be measured. Each ion trap was used to trap single $^{88}Sr^{+}$ ions, and the ions were cooled to their motional ground state by a combination of Doppler cooling and sideband cooling. Once fully cooled, electric field noise was measured by observing the change in thermal occupation number over a chosen time period. The rate of electrode charging was measured by observing the micromotion amplitude change with respect to time as the electrodes were irradiated with laser light.

7.1.1 Electric Field Noise

Anomalous noise was not expected to have any dependencies on chemical composition at cryogenic temperatures; the measured electric field noise supports this claim. Electric field noise in aluminum traps was on the order of the Johnson noise, demonstrating that the anomalous noise had been fully suppressed in these traps. These heating rates matched rates observed in gold traps in prior work, demonstrating that aluminum traps could match the performance of gold traps. The copper ion trap exhibited heating rates an order of magnitude larger than the predicted Johnson noise, suggesting that anomalous noise had not been completely suppressed. Further work is required to determine if the noise can be further reduced in copper traps.

Aluminum traps were prepared with 5, 10, and 20 nm of aluminum oxide deposited onto the electrode surface to measure the effects of oxide growth on electric field noise. Heating rate measurements suggest that the electric field noise is highly dependent upon oxide thickness. Measurements appeared to indicate that the noise saturates with a characteristic distance of $\delta = 13 \pm 3$ nm. The trap with 10 nm of deposited oxide had unusually large noise; the trends indicate that it should be possible to further reduce the anomalous noise in this trap. If anomalous noise is significantly reduced, it is possible that the heating rate would exhibit linearly growth with oxide thickness rather than exponential. More careful measurements of electric field noise in aluminum oxide coated traps should be taken in the future to further characterize this noise.

7.1.2 Light-Induced Charging

The lasers used in this experiment were not expected to charge any electrode surfaces due to their relatively low photon energies. Experimental data contradicted this prediction, with aluminum and aluminum oxide electrodes charging when irradiated with 405 nm light and copper electrodes charged when exposed to 674 nm light. The time constants for electrode charging before saturation was approximately $\tau = 600$ seconds for aluminum and $\tau = 140$ seconds for copper. The addition of aluminum oxide to the aluminum electrodes changed the time constant to $\tau = 500$ seconds; however, the existence of a native oxide layer on typical aluminum surfaces (including the aluminum trap tested) indicates that this is more likely to be a function of a different fabrication method used for the aluminum oxide traps.

The electrode charging was described within the framework of the theory presented in Chapter 4; unfortunately this proved insufficient to fully describe the data. While the concepts of band bending sufficiently described the charging seen in copper traps, it did not explain the absence of charging due to the 405 nm and 460 nm light; a preliminary hypothesis is the existence of absorption-based phenomena. Band bending did not provide an explanation for the charging of aluminum electrode, but the required charge density on the surface of the electrodes to induce photoemission was calculated to be on the order of 3.5 eV from the band bending model. The presence of such a surface charge would completely explain the phenomena observed in aluminum electrodes; however, the theory presented in this thesis is insufficient to describe a mechanism for such charge.

Increased micromotion was observed in trapped ions even after the incident laser beam was removed, indicating that the charge dissipation rate is much slower than the charge creation rate. This would indicate that the charge dissipation mechanism is not the rate-limiting factor, otherwise the charge dissipation rate would be significantly faster in order to create a saturation of charge on the surface. Such data suggests that the surface charge is due to trapped charges on the oxide, and that an increase in surface charge creates a barrier for photoelectrons to overcome. This is consistent

with the theory presented in this document.

The final inconsistency observed is the difference between incident photon flux, lattice sites, and charge creation. If photoemission was the true source of surface electrode charging, then the charging rate should be rate-limited by photon flux or the number of available lattice sites on the surface. A charging rate on the order of 10^4 charges per second was observed; this is 8 orders of magnitude lower than the number of available lattice sites on the surface layer and 28 orders of magnitude smaller than the incident photon flux on the irradiated surface. These results imply some efficiency ratio that determines how many incident photons truly induce photoemission.

7.2 Future Work

This thesis has laid down the groundwork for a variety of future experiments. The ion trap fabrication process described in this thesis has proven to be robust and versatile, opening up the possibility of fabricating ion traps out of a host of interesting and novel materials. Potential electrode materials include semiconductors to provide finer control over conductivity and electron mobility and further compatibility with current integrated circuit technology and superconductors so that the surfaces can be shielded from internal defect structure. The theorized dependence of anomalous noise on defect structure also provides a convincing argument for more post-processing techniques being incorporated into the microfabrication in order to more finely control the microstructure.

In addition to these studies in noise, further work is required to characterize and understand the full mechanism behind light-induced charging. In particular, more quantitative data is needed on the effects of surface physics on photoemission. Both oxide layer thickness and potential adsorbates have been proposed as causes for the unexpected photoemissivity of aluminum and copper, but neither mechanism is fully satisfying. The observed results suggest that surface physics will become increasingly important in ion trapping as traps scale down and irradiation of the electrodes by control optics becomes more common, indicating the necessity of further research into

this charging phenomena.

Appendix A

Experimental Setup

After an ion trap has been fabricated, several factors must be addressed before it can be successfully operated. Collisions with background gas can prevent ions from being trapped, and such interactions can disturb the precision control that is desired; therefore a vacuum environment is desired. Once a vacuum environment is achieved, the ions must be sourced and trapped within the confining potential. Finally, there must be sufficient optical access in the trapping apparatus to allow for cooling of the trapped ions, and eventually for measurements to be taken.

This chapter details the practical aspects of ion trapping, from the operation of a cryogenic vacuum environment to the implementation of ion measurements. This section details enough about the apparatus such that the experiments described in this thesis may be understood; for a more complete reference on the design and operation of the apparatus, see Reference [Lab08].

A.1 Experimental Apparatus

A.1.1 Cryostat

The ion trap is operated inside of a bath cryostat consisting of a vacuum enclosure and insulated tanks of cryogens. The addition of cryogens allows a sufficient experimental vacuum pressure (10^{-10} Torr) to be reached much more easily; at cryogenic tempera-

tures outgassing is suppressed, allowing the use of a wider of range of materials while still maintaining an ultra high vacuum (UHV) environment.

The inside of the cryostat holds a 1.4 L tank for liquid nitrogen and a 1.75 L tank for liquid helium. The liquid helium tank is surrounded by a 77K thermal shield (cooled by the liquid nitrogen tank) in order to reduce the thermal load on the liquid helium. Between the bottom of the liquid helium tank and the thermal shield is the experimental work space, shown in Figure A-1. The trap (center) is mounted to the base plate of the liquid helium tank, where it is held at 4 Kelvin. In addition, the trap is sandwiched between two superconducting niobium rings, which both stabilize the magnetic field in the trapping area and prevent Zeeman splitting of the $5S_{1/2} \rightarrow 4D_{5/2}$ transition. The entire chamber is pumped down to a vacuum using a turbo pump.

The outer shell of the cryostat has 4 symmetrically spaced 50 mm openings (shown in Figure A-1); three of these provide optical access to the vacuum chamber and the last (right in Figure A-1) provides access for all of the experiment's electrical connections. There is a final opening on the bottom of the cryostat which provides access for the camera, photomultiplier tube (PMT), and imaging optics. The entire cryostat is mounted in a support structure surrounded by three breadboards to provide space for optics.

A.1.2 Optics

The experiment uses six lasers – the four covered in Chapter 3 plus 405 nm and 460 nm lasers to ionize neutral strontium. The first five lasers are all available as laser diodes; the sixth, 460 nm, is produced by frequency-doubling a 920 nm laser. After frequency stabilization, the lasers are coupled into optical fibers – the 405 nm and 460 nm lasers are coupled into the same fiber, as are the infrared lasers. The optical fibers deliver the lasers to the optics table surrounding the cryostat, shown in Figure A-2.

The 422 nm is used for Doppler cooling the trapped ion; in order to fully cool the ion, the ion must be cooled in three axes. The 422 nm is split into two orthogonal components which then recombine at the trap center, providing projections onto two

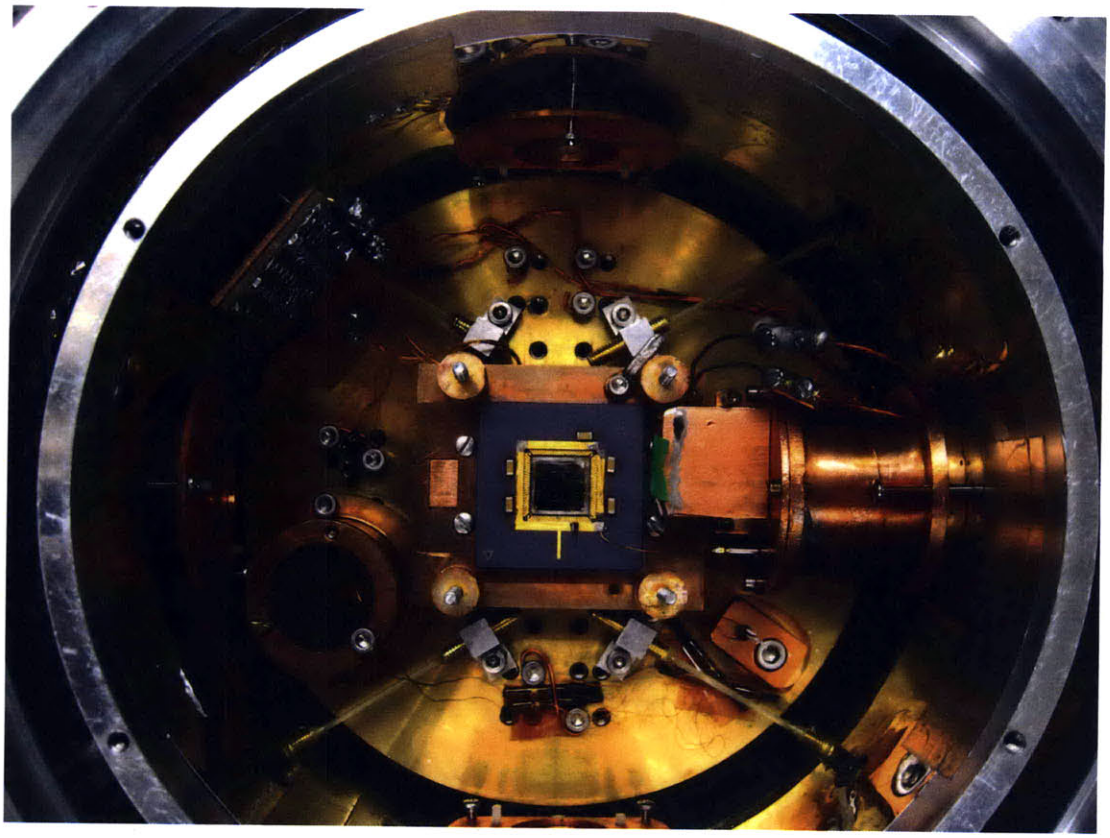

Figure A-1: The experimental work space underneath the liquid helium tank. The fully packaged trap lies in the center of the trap. Windows on the top, left, and bottom of the shell provides optical access, and to the right is the radiofrequency resonator that drives the trap potential and provides access for the electronics that control the trap.

of the three axes. The asymmetry of the trapping potential provides a projection onto the third axis, so all three axes can be cooled simultaneously. Sideband cooling is an isotropic process, so cooling is only needed in one axis.

The lasers must be aligned with the trap to ensure that the trapped ion receives light. The height of the trapped ion can be computed numerically, and the beamwidth of the laser allows for some error in this placement. Therefore the lasers only need to be aligned in the radial and axial directions (perpendicular and parallel to the ground electrode, respectively). This is accomplished by lowering the lasers until light is scattering off of the trap electrodes, as in Figure A-3. The lasers can then be aligned in the x-y plane and then raised to the appropriate height.

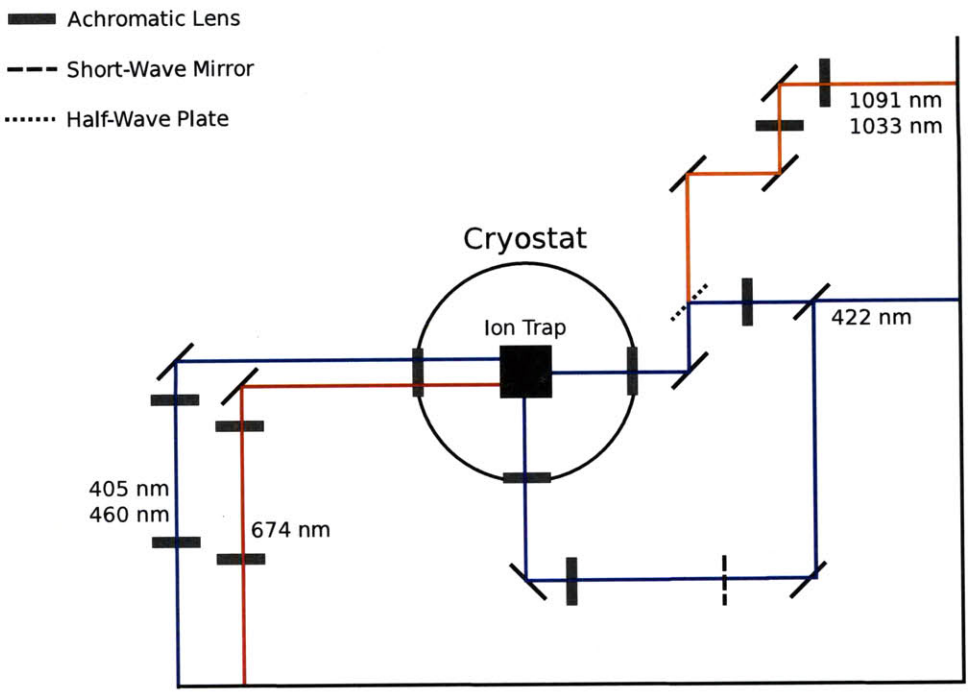

Figure A-2: The laser optics setup surrounding the cryostat. The 405 nm and 460 nm laser are coupled together into the same fiber, as are the 1033 nm and 1091 nm lasers.

The final component of the optics is the imaging system. Imaging and photon detection is accomplished by focusing scattered light through the bottom opening of the cryostat. The scattered light goes through a notch filter that blocks all lights except 422 ± 5 nm; this reduces noise from the environment and allows only the 422 transition to be seen. The remaining light goes through a 70/30 beamsplitter that delivers 70% of the light to a photomultiplier tube for photon counting, and the remaining 30% to a CCD camera. The CCD camera allows for detection of fluorescence and scattering of the lasers on the electrode surface, while the photomultiplier tube provides a more sensitive tool for detecting fluorescence during cooling. The images in Figures A-3 and A-4 were taken using the CCD camera.

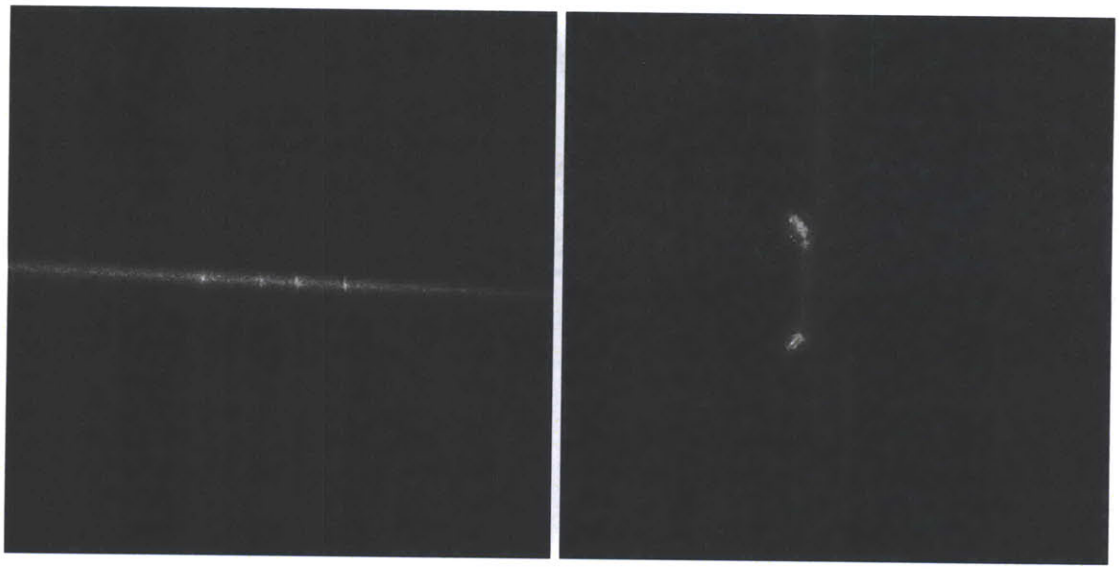

Figure A-3: Demonstration of aligning the radial (left) and axial (right) lasers by scattering light directly off the trap surface. The narrowest part of the middle electrode is 150 μm wide.

A.2 Trapping Ions

A.2.1 Loading

The first step in trapping ions is providing a source of ions. This experiment uses evaporation of strontium in a resistive oven as a source of neutral atoms in the vapor phase. Strontium metal is placed inside a stainless tube with two strips of stainless foil as a heating element. Approximately 5 Amps of current is passed through the foil to heat up the strontium until it evaporates. The entire oven is mounted in a copper enclosure to act as a heat sync, and this is heat sunk to 77 K to reduce the thermal load on the helium tank.

The neutral strontium is then photoionized in a two step process. First the 460 nm laser is used to excite a transition to the $4P$ orbital, and then any laser with wavelength lower than 413 nm can be used to remove the excited electron from electronic confinement. Alternatively, there is a 405 nm transition that is autoionizing [MBK95]; therefore the ionization process can be optimized by using a 405 nm laser as the second ionizing laser. The ionizing lasers are aligned to the trap's center such that

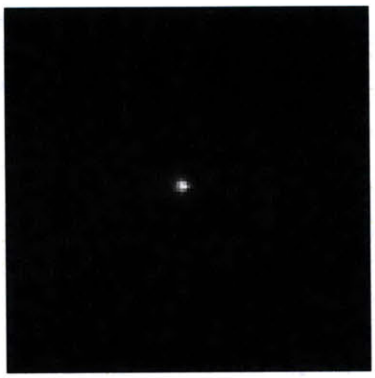

Figure A-4: An image of a trapped ion fluorescing, as taken by the CCD camera.

the ionized strontium atoms can be immediately trapped and cooled post-ionization.

Trapped ions are detected using the 422 nm transition, as shown in Figure A-4. Any ions that remain trapped within the potential field will fluoresce due to the presence of the 422 nm laser; the emitted photons are then captured by the CCD camera and the PMT. It is possible to trap multiple ions simultaneously; this can be dealt with by manipulating the compensation voltages until an ion "falls" out of the potential.

A.2.2 Compensation

Compensation, outlined in Section 3.4.2, is used to minimize the micromotion of trapped ions. Properly compensating the trapped ion is performed using fluorescence from the $5S_{1/2} \rightarrow 4P_{1/2}$ and the imaging optics outlined in Section A.1.2. Micromotion is observed as a smearing of the ion on the CCD camera due its fast motion, and as a periodic fluctuation in the fluorescence on the photon counter. Using the imaging optics as visual cues, appropriate compensation voltages can be determined. Typical compensation voltages are 5 to 10 Volts for the endcaps and -5 to -13 Volts for the middle electrodes.

Bibliography

[Ara09] Aram W. Harrow, Avinatan Hassidim, and Seth Lloyd. Quantum algorithm for solving linear systems of equations. 2009.

[BMB+98] D. J. Berkeland, J. D. Miller, J. C. Bergquist, W. M. Itano, and D. J. Wineland. Minimization of ion micromotion in a paul trap. *J. Appl. Phys.*, 83:5025, 1998.

[CBB+05] J. Chiaverini, R. B. Blakestad, J. Britton, J. D. Jost, C. Langer, D. Liebfried, R. Ozeri, and D. J. Wineland. Surface-electrode architecture for ion-trap quantum information processing. *Quantum Inf. Comput.*, 5:419, 2005.

[CZ95] J. I. Cirac and P. Zoller. Quantum computations with cold trapped ions. *Phys. Rev. Lett.*, 74:4091, 1995.

[DH81] P. Dutta and P.M. Horn. Low frequency fluctuations in solids: 1/f noise. *Rev Mod Phys*, 53:497, 1981.

[DOS+06] L. Deslauriers, S. Olmschenk, D. Stick, W. K. Hensinger, J. Sterk, and C. Monroe. Scaling and suppression of anomalous heating in ion traps. *Phys. Rev. Lett.*, 97:103007, 2006.

[Ear42] Samuel Earnshaw. On the nature of the molecular forces which regulate the constitution of the luminiferous ether. *Trans. Camb. Phil. Soc*, 7:97–112, 1842.

[Fey82] R. P. Feynman. Simulating Physics with Computers. *Intl. J. Theor. Phys.*, 21:467, 1982.

[Flo83] Gaston Floquet. Sur les quations diffrentielles linaires coefficients priodiques. *Ann. Ecole Norm Sup.*, 12:47–88, 1883.

[GGJM+06] N. Gaillard, M. Gros-Jean, D. Mariolle, F. Bertin, and A. Bsiesy. Method to assess the grain crystallographic orientation with a submicronic spatial resolution using kelvin probe force microscope. *Appl. Phys. Letters*, 89:154101, 2006.

[Hou08] M. G. House. Analytic model for electrostatic fields in surface-electrode traps. *Phys. Rev. A*, 78, 2008.

[Joh28] J.B. Johnson. Thermal agitation of electricity in conductors. *Phys. Rev.*, 32:97–109, 1928.

[JP87] J. Clarke J. Pelz. Quantitative local interference model for 1/f noise in metal films. *Phys Rev*, B36:4479, 1987.

[Kap51] P. L. Kapitsa. Dynamic stability of a pendulum with a vibrating point of suspension. *Zh. Eksp. Teoret. Fiz.*, 21:588–598, 1951.

[Lab08] J. Labaziewicz. *High Fidelity Quantum Gates with Ions in Cryogenic Microfabricated Ion Traps.* PhD thesis, Massachusetts Institute of Technology, Cambridge, MA, 2008.

[LGA+08] J. Labaziewicz, Y. Ge, P. Antohi, D. Leibrandt, K. R. Brown, and I. L. Chuang. Suppression of heating rates in cryogenic surface-electrode ion traps. *Phys. Rev. Lett.*, 100:013001, 2008.

[LGL+08] J. Labaziewicz, Y. Ge, D. Leibrandt, S. X. Wang, R. Shewmon, and I. L. Chuang. Temperature dependence of electric field noise above gold surfaces. *Phys. Rev. Lett.*, 101:180602, 2008.

[Mac47] Norman William MacLachlan. *Theory and Application of Mathieu Functions.* Clarendon Press, Oxford, 1947.

[Mat68] Emile Mathieu. Mmoire sur le mouvement vibratoire dune membrane de forme elliptique. *Journal des Mathmatiques Pures et Appliques*, pages 137–203, 1868.

[MBK95] W. Mende, K. Bartschat, and M. Kock. Near-threshold photoionization from the Sr I (5s5p) $^1P_1^0$ state. *J. Phys. B*, 28:2385, 1995.

[MDW08] J. Mikosch S. Trippel N. Morrison M. Reetz-Lamour P. Woias R. Wester M. Debatin, K. Kröner and M. Weidemüller. Planar multipole ion trap. *Phys. Rev. A*, 77, 2008.

[Miy01] Seiichi Miyzaki. Photoemission study of energy-band alignments and gap-state density distributions for high-k gate dielectrics. *J. Vac. Sci. Technol. B*, 19(6), 2001.

[Nyq28] H. Nyquist. Thermal agitation of electricity in conductors. *Phys. Rev.*, 32:110–113, 1928.

[OCK+06] S. Oh, K. Cicak, J. S. Kline, M. A. Sillanp, K. D. Osborn, J. D. Whittaker, R. W. Simmonds, and D. P. Pappas. Elimination of two level fluctuators in superconducting quantum bits by an epitaxial tunnel barrier. *Phys. Rev. B*, 74:100502, 2006.

[Pau90] W. Paul. Electromagnetic traps for charged and neutral particles. *Rev. Mod. Phys.*, 62:531–540, 1990.

[PS53] W. Paul and H. Steinwedel. Ein neues massenspektrometer ohne magnetfeld. *Z. Naturforsch. A*, 8:448, 1953.

[Ray02] A.K. Raychaudhuri. Measurement of 1/f noise and its application to materials science. *Curr Opin Solid State Mater Sci*, 6:67–85, 2002.

[RBB+06] N. A. Robertson, J. R. Blackwood, S. Buchman, R. L. Byer, J. Camp, D. Gill, J. Hanson, S. Williams, and P. Zhou. Kelvin probe measurements: investigations of the patch effect with applications to ST-7 and LISA. *Class. Quant. Grav.*, 23:2665, 2006.

[RHS+08] T. Rosenband, D. B. Hume, P. O. Schmidt, C. W. Chou, A. Brusch, L. Lorini, W. H. Oskay, R. E. Drullinger, T. M. Fortier, J. E. Stalnaker, S. A. Diddams, W. C. Swann, N. R. Newbury, W. M. Itano, D. J. Wineland, and J. C. Bergquist. Frequency ratio of Al^+ and Hg^+ single-ion optical clocks; metrology at the 17th decimal place. *Science*, 319:1808, 2008.

[Ric06] Philip J. Richerme. Measurements of $^{88}Sr^+$ ions in a linear paul trap. Bachelor's Thesis, 2006.

[RO92] F. Rossi and G. I. Opat. Observations of the effects of adsorbates on patch potentials. *J. Phys. D*, 25:1349, 1992.

[SBC+93] C. I. Sukenik, M. G. Boshier, D. Cho, V. Sandoghdar, and E. A. Hinds. Measurement of the Casimir-Polder force. *Phys. Rev. Lett.*, 70:560, 1993.

[Sch18] W. Schottky. ber spontane stromschwankungen in verschiedenen elektrizittsleitern. *Annalen der Physik*, 57:541–567, 1918.

[Sem69] Yu. I. Semov. Work function of oxidized metal surfaces and estimation of al_2o_3 film band structure paramters. *Phys. Stat. Sol.*, 32, 1969.

[SF86] A.D. Stone S. Feng, P.A. Lee. Sensitivity of the conductance fluctuation of a disordered metal to the motion of a single atom: Implications for 1/f noise. *Phys Rev Lett*, 56:1960, 1986.

[Sho97] P. W. Shor. Polynomial-time algorithms for prime factorization and discrete logarithms on a quantum computer. *SIAM J. on Comp.*, 26:1484, 1997.

[TKK+00] Q. A. Turchette, D. Kielpinski, B. E. King, D. Liebfried, D. M. Meekhof, C. J. Myatt, M. A. Rowe, C. A. Sackett, C. S. Wood, W. M. Itano, C. Monroe, and D. J. Wineland. Heating of trapped ions from the quantum mechanical ground state. *Phys. Rev. A*, 61:063418, 2000.

[TST97] K.M. O'Hara T.A. Savard and J.E. Thomas. Laser-noise-induced heating in far-off resonance optical traps. *Phys Rev A*, 56(2):1095–1098, 1997.

[Wei87] M.B. Weissman. 1/f noise and other slow, non-exponential kinetics in condensed matter. *Rev Mod Phys*, 60:537, 1987.

[WIBH87] D. J. Wineland, W. M. Itano, J. C. Bergquist, and R. G. Hulet. Laser-cooling limits and single-ion spectroscopy. *Phys. Rev. A*, 36:2220, 1987.

[WMI+98] D. J. Wineland, C. Monroe, W. M. Itano, D. Leibfried, B. E. King, and D. M. Meekhof. Experimental issues in coherent quantum-state manipulation of trapped atomic ions. *J. of Res. of the National Inst. of Standards and Technology*, 103:259, 1998.

[YCD89] H. Wallis Y. Castin and J. Dalibard. Limit of doppler cooling. *J. Opt. Soc. Am. B*, 6(11):2046–2057, 1989.